RSC Advances

‘Nano-ZnO impregnated inorganic-polymer hybrid thin film nanocomposite nanofiltration membranes: An investigation of variation in structure, morphology and transport properties’

Journal:	*RSC Advances*
Manuscript ID:	RA-ART-11-2014-014854.R2
Article Type:	Paper
Date Submitted by the Author:	11-Mar-2015
Complete List of Authors:	Pal, Avishek; Bhabha Atomic Research Centre, Desalination Division Dey, T. K.; Bhabha Atomic Research Centre, Desalination Division Singhal, Anshu; Bhabha Atomic Research Centre, Chemistry Division Bindal, R.C.; Bhabha Atomic Research Centre, Desalination Division Tewari, P.K.; Bhabha Atomic Research Centre, Desalination Division

Cite this: DOI: 10.1039/c0xx00000x

www.rsc.org/xxxxxx

ARTICLE TYPE

Nano-ZnO impregnated inorganic-polymer hybrid thin film nanocomposite nanofiltration membranes: An investigation of variation in structure, morphology and transport properties

Avishek Pal,[a] T. K. Dey,*[a] Anshu Singhal,[b] R. C. Bindal[a] and P. K. Tewari[a]

[a]Desalination Division, [b]Chemistry Division

Bhabha Atomic Research Centre, Trombay, Mumbai, India- 400085

Received (in XXX, XXX) Xth XXXXXXXXX 20XX, Accepted Xth XXXXXXXXX 20XX
DOI: 10.1039/b000000x

Inorganic–polymer hybrid thin film nanocomposite nanofiltration (TFN-NF) membranes prepared by *in-situ* interfacial polymerization of branched polyethyleneimine and trimesoyl chloride, with simultaneous impregnation of as synthesized hexagonal wurtzite ZnO nanocrystals (nano-ZnO), either through aqueous or organic phase, have been extensively characterized. No occurrence of inter-atomic charge transfer between the nano-ZnO and the host polyamide matrix, revealed by X-ray photoelectron spectroscopy and however, formation of noncovalent type secondary chemical interactions with peripheral hydroxyl groups of nano-ZnO and the polyamide network, substantiated through ATR FTIR analysis infer about the base of interaction present within the skin layer nanocomposite polyamide matrix of the membranes. Scanning electron microscopy revealed the formation of distinct patterns and coils, through multiple-point secondary chemical interactions between the nano-ZnO and the polyamide network, in the membranes' skin surfaces when introduced through aqueous amine phase. However, when introduced through the organic phase, nanomaterials remained distributed as discrete clusters within membrane skin layer because of lack of polar environment around the reaction zone, further emphasizing the function of medium in which the nanomaterials are incorporated. Atomic force microscopy showed the variation of surface roughness features with change in the precursor medium of introduction of nano-ZnO. Nanofiltration performance towards different solutes, providing differential rejections in the order of $MgCl_2$ > NaCl ≥ Na_2SO_4, revealed that the membranes are distinctly positively charged. Solvent fluxes of the membranes were significantly higher when nanomaterials were introduced through aqueous phase as compared to the organic phase.

1 Introduction

Pressure driven nanofiltration (NF) membrane processes have become significantly useful in recent years in the field of aqueous stream separations. They offer exciting options for various industrial applications due to their ability to achieve high selectivity between mono and multivalent ionic species from mixed electrolyte streams with additional advantages like low transmembrane pressure, low operational cost and high permeate flux.[1,2] Thin film composite (TFC) type membranes having an ultrathin selective barrier layer, generally produced by *in-situ* interfacial polycondensation of reactive monomers on a suitable substrate material, constitute the majority of commercially available polymeric nanofiltration membranes. The barrier skin layer, made of synthetic polymeric materials, additionally and preferentially containing either negative or positive charge bearing functionalities, influences the separation behaviors of the membrane, by preferentially retaining certain components and allowing the passage of some other, depending on the interaction between surface charge of the membrane and charges of the solutes under consideration.[3,4] The major areas of applications of these membranes include bulk wet stream processing such as water purification for production of drinking water, effluent treatment for removal of toxic elements,[5] dairy industries,[6] food and pharmaceutical industries,[7,8] textile industries,[9] biotechnological industries,[10] etc.

For almost a decade, when it seemed that the performance of the membranes in tems of solute rejection and especially the solvent flux, had reached the limits, the advent of nanotechnology provided a new dimension to the scientists by changing the scenario.[11] Membranologists explored promising ways to

Cite this: DOI: 10.1039/c0xx00000x
www.rsc.org/xxxxxx

ARTICLE TYPE

prevail over some of the limitations associated with the synthetic polymeric membranes by developing new types of organic-inorganic hybrid nanocomposite materials.[12-14] Extensive research works on various metals, metal oxides as well as ceramic and zeolite nanoparticles have been conducted to impart improved physicochemical properties in the membranes. Production of membranes by incorporation of nanomaterials tendered better chemical, mechanical and thermal resistance and also prevented adhesion as well as adsorption of the undesired fouling materials on their surfaces, thereby maintaining the membrane permeability and selectivity as well as minimizing the load on pretreatment and chemical cleaning. It has been observed that microstructural features of the membranes are affected by site specific interaction between the metal oxide nanoparticle and the host polymer matrix, altering the skin layer morphology, pore size, pore size distribution, surface roughness, etc. which eventually influence their performances. Different metal oxide nanoparticles like silica (SiO_2),[15,16] alumina (Al_2O_3),[17,18] titania (TiO_2),[19-21] ferric oxide (Fe_2O_3),[22] zinc oxide (ZnO),[23,24] zeolites,[25,26] etc. have been employed as nanofillers in nanocomposite membranes' polymeric host matrix leading to promising improvements like better chemical and thermomechanical properties.

In recent times, ZnO nanoparticles has drawn much attention of the membranologists as a suitable nontoxic, bio-safe and bio-compatible material with strong inhibitory and antibacterial effect, over a broad spectrum, of both G^+ and G^- bacteria.[27-29] Adams et al.,[30] Brayner et al.[31] and Jeng and Swanson[32] have reported that ZnO is more efficient in controlling the growth of micro-organisms than other metal oxides such as SiO_2, MgO, TiO_2 and CaO by significantly inhibiting the growth of a wide range of pathogenic bacteria under visible light conditions. The commonly proposed antimicrobial mechanisms for nano-ZnO are i) generation of reactive oxygen species like hydrogen peroxide (H_2O_2), hydroxyl radical ($^{\cdot}OH$) and singlet oxygen ($^1O_2$) from the surface of zinc oxide, penetrating the cell membrane and inhibiting the growth of the cells and ii) rupture of cell membrane and leakage of cytoplasmic content because of binding between the bacterial cell and ZnO nanoparticles due to electrostatic forces.[33-35]

The present study emphasizes on investigations of structural and physicochemical features of the inorganic-polymer hybrid thin film nanocomposite nanofiltration (TFN-NF) membranes, prepared by impregnation of as synthesized nano-ZnO into the polymer skin layer during the *in-situ* interfacial polycondensation of branched polyethyleneimine (PEI) and trimesoyl chloride (TMC). The synthesized nano-ZnO have been characterized by X-ray powder diffraction (XRD) analysis, Fourier Transform Infra-red (FTIR) spectroscopy, Raman spectroscopy and X-ray photoelectron spectroscopy (XPS). For membranes, XPS as well as ATR FTIR analysis of skin layers investigated the influence of nano-ZnO, with variation in the ways of incorporation, on the electronic and molecular level interactions happenning within the nanocomposite polyamide matrices of the TFN-NF membranes. Changes in skin surface morphologies of the skin layer of nanocomposite membranes have been investigated by scanning electron microscopy (SEM). Quantitative surface roughness analysis by atomic force microscopy (AFM) has been applied to probe the role of the nanomaterials in influencing the membrane topographies. Energy dispersive X-ray (EDX) analysis has been employed to determine the elemental composition of skin layer of the TFN-NF membranes. Cross-flow permeation experiments have been performed to correlate the variation in physicochemical features of the membranes with their transport parameters like solute rejection and solvent flux behaviors.

Cite this: DOI: 10.1039/c0xx00000x

www.rsc.org/xxxxxx

2 Experimental section

2.1 Materials

Polysulfone (Psf; M_W: 30,000 Da), procured from Solvay Speciality Polymers (India), N-methyl-2-pyrrolidone (NMP) with a relative vapor density of 3.4 (vs air) and purity of ≥ 99 %, procured from Sigma-Aldrich and polyvinyl pyrrolidone (PVP, K-30; M_W: 40,000 Da), procured from SRL (India), were used for preparation of the polysulfone (Psf) base membrane. The nonwoven porous polyester fabric used as a reinforcement material for making the base membrane had a density of 75 g/m^2 and a thickness of 110 µm with an air permeability of 70 dm^3/m^2 at 2 mbar. Aqueous solution (50 w/v %) of branched poly(ethyleneimine) (PEI; M_W: 600,000-1,000,000 Da; d_4^{20}: 1.08), typically constituting about 25 % primary, 50 % secondary and 25 % tertiary amine groups and trimesoyl chloride (TMC) with 98 % purity, procured from Sigma-Aldrich were used without any further purification. The organic solvent, extrapure (99 %) AR grade n-hexane was procured from SRL, India. Various electrolytes of AR grade, like magnesium chloride heptahydrate ($MgCl_2.7H_2O$), anhydrous sodium sulphate (Na_2SO_4) and sodium chloride (NaCl) were obtained from different companies in India. The conductivity of ultra pure water used for preparation of monomer solutions, membrane preparation as well as nanofiltration experiments was below 2µS/cm. Zinc(II) acetylacetonate hydrate (99.995 % purity) [$Zn(acac)_2.H_2O$] was obtained from Sigma-Aldrich.

2.2 Synthesis of ZnO nanocrystals

ZnO nanocrystals (nano-ZnO) were synthesized by thermal decomposition of anhydrous Zn(acetylacetonate)$_2$ in n-octylamine at temperature as low as 110 °C. The precursor anhydrous Zn(acetylacetonate)$_2$ was prepared following the method of Rudolph and Henry.[36] In a typical preparation, 0.5 g (1.89 mmol) of anhydrous Zn(acetylacetonate)$_2$ was taken in a 50 mL three-neck flask with 10 mL (~60.5 mmol) of n-octylamine. The reaction flask was evacuated to a vacuum level of 2 mbar for 30 minutes at 40 ^{o}C. The reaction system was then heated (~10 ^{o}C min^{-1}) to 110 ^{o}C under argon flow and maintained at this temperature for 2 hours. A white suspension was obtained which was cooled to 60 ^{o}C and 5 mL of methanol was added to the reaction flask. The nanocrystals of ZnO were recovered by centrifugation, dispersed in toluene, and precipitated by addition of methanol. The redispersion and precipitation steps were repeated twice to remove any unreacted precursors and excess solvent.

2.3 Preparation of Psf base membrane

The flat-sheet microporous Psf base membrane was prepared following nonsolvent induced phase inversion method, where a homogeneous casting solution, comprising of 30 (w/v) % Psf in NMP, along with the pore forming additive - PVP (40 w/w % of Psf), was cast on a nonwoven polyester substrate to a thickness of 100 μm using an automated casting machine. The membrane was immediately dipped in a water bath, maintained at room temperature, for immersion precipitation. The water of the bath was changed several times to ensure a complete removal of the solvent (NMP) and additive (PVP) from the membrane matrix by leaching. The entire casting machine was kept in an environmentally controlled atmosphere where temperature and relative humidity were maintained at 25 ^{o}C and 35-40 %, respectively. This Psf membrane was subsequently used as a base material for preparation of the thin film nanocomposite nanofiltration (TFN-NF) membranes.

2.4 Preparation of Control-NF and inorganic-polymer hybrid TFN-NF membranes

A control, thin film composite nanofiltration membrane, (Control-NF), devoid of any nanomaterial, was prepared by *in-situ* interfacial polycondensation reaction (Scheme 1) between PEI (in aqueous medium) and TMC (in organic, n-hexane medium). A piece of microporous Psf base membrane was

Cite this: DOI: 10.1039/c0xx00000x

www.rsc.org/xxxxxx

treated with 4 (w/v) % aqueous solution of PEI for 4 minutes. After removing the amine soaked base membrane from the aqueous medium and eliminating the excess solution by gently squeezing it between two rubber rollers the membrane was dipped in a 0.1 (w/v) % TMC solution for 30 seconds. The nascent TFC membrane, comprising of a freshly deposited ultrathin polyamide film over the surface of the Psf base membrane was further heat cured at 90 ^{o}C in a hot air circulated oven for 30 minutes.

For development of the inorganic-polymer hybrid TFN-NF membranes, the nano-ZnO was introduced in either aqueous or organic phase. The nano-ZnO was dispersed in aqueous or n-hexane medium by applying ultrasonication for 15 minutes prior to the start of membrane making process. When prepared by incorporation of the nano-ZnO through the aqueous phase, 4 (w/v) % aqueous solutions of PEI containing well dispersed nano-ZnO of varying concentrations of 0.05, 0.1 and 0.2 (w/v) % were used. The membranes were prepared using the same procedure as the Control-NF, by performing *in-situ* interfacial polycondensation reaction with 0.1 (w/v) % TMC solution (Schematics in Fig. 1a), followed by curing at 90 ^{o}C for 30 minutes. These membranes were named as Aq-ZnO:TFN-NF-1, Aq-ZnO:TFN-NF-2 and Aq-ZnO:TFN-NF-3, respectively.

Similarly, in another set of experiments, nano-ZnO of various concentrations of 0.05, 0.1 and 0.2 (w/v) % were ultrasonically dispersed in n-hexane, containing 0.1 (w/v) % TMC monomer. The *in-situ* interfacial polycondensation was conducted adopting the same approach as the Control-NF, with 4 (w/v) % aqueous PEI solution (Schematics in Fig. 1b), followed by curing at 90 ^{o}C for 30 minutes. These membranes were named as Org-ZnO:TFN-NF-1, Org-ZnO:TFN-NF-2 and Org-ZnO:TFN-NF-3, respectively. They were washed with de-ionized water to remove the leachable chemicals before conducting performance evaluation tests.

2.5 Textural and structural characterizations of as synthesized nano-ZnO

Phase purity and structure of the ZnO nanocrystals were determined by X-ray powder diffraction (XRD) data, which were collected on a Philips X'Pert pro X-ray diffractometer using Cu-Kα radiation ($\lambda = 1.5418$ Å) at 40 kV and 30 mA.

FTIR spectrum of the ZnO nanocrystals was recorded in attenuated total reflectance (ATR) mode using a Bruker Vertex 70 FTIR spectrometer, in the range of 500–1500 $\mathrm{cm^{-1}}$.

Micro-Raman spectra of the nanocrystals were obtained on a LABRAM-I, ISA make spectrometer using an Ar^+ ion laser (488 nm) equipped with a Peltier-cooled CCD detector.

For XPS characterization of the ZnO nanocrystals, a DESA-150 electron analyzer (Staib Instruments, Germany) equipped with Mg-Kα X-ray source (1253.6 eV) was employed. The spectrometer's binding energy scale was calibrated with Au-$4f_{7/2}$ photopeak at a binding energy (BE) of 83.95 eV. Curve fitting of intensity versus binding energy (BE) plots comprising the multiplex photo peaks was performed employing a least-squares peak analysis software (XPSPEAK 4.1). Using the Gaussian/Lorentzian sum function, peak areas as well as corresponding full width at half maximum (FWHM) were also determined for the high resolution Zn-2p and O-1s spectra. The fitting error in both peak position and FWHM are ~ 0.1 eV.

2.6 Characterization of TFN-NF membranes

2.6.1 Characterization of skin layers of TFN-NF membranes by XPS

XPS was employed for quantitative evaluation of chemical interactions, in the skin layer polymer matrix of the TFN-NF membranes. The skin layer was characterized and compared in terms of change in core level BE values of N, O and Zn for Control-NF, Aq-ZnO:TFN-NF and Org-ZnO:TFN-NF class

Cite this: DOI: 10.1039/c0xx00000x

www.rsc.org/xxxxxx

ARTICLE TYPE

of membranes. The curve fitting for N-1s, O-1s and Zn-2p were done by employing the XPSPEAK 4.1 software. For validation of proper fitting of the curves in all the spectra, values of fitting parameter, χ^2 (Kai square) were evaluated, since χ^2 having value below 5.0 is acceptable. The fitting error in both peak position and FWHM are ~ 0.1 eV.

2.6.2 Spectral characterization of skin layers of TFN-NF membranes by FTIR spectroscopy

Bruker Vertex 70 FTIR spectrometer, equipped with an ATR attachment (ZnSe crystal, 45^o angle of incidence and refractive index 2.4), was employed for ATR-FTIR analysis of membranes. The membrane's skin surface was kept faced down onto the ATR crystal element and a light pressure was applied using a MIRacle high pressure clamp with torque-limited press. The radiation penetration depth was 2 μm. All infrared spectra were recorded in transmittance mode, in the range of 600-4000 cm^{-1}, at 25 ^oC. Evaluation of each spectra was done by acquiring 100 scans at a spectral resolution of 2 cm^{-1}.

2.6.3 Morphological investigation of TFN-NF membranes by SEM

The morphological analyses, through SEM, of ultrathin skin surfaces of the TFN-NF membranes were carried out using CamScan–CS3200LV, UK. In order to make the membranes electrically conducting, 2 mm × 2 mm strips of the dry membrane samples were sputter coated on the skin surface with gold-palladium alloy for 60 seconds employing a current of 30 mA. The skin layer images were recorded at an acceleration voltage of 15 kV and 4000X magnification when operated in secondary electron mode. For acquiring the cross-sectional images of the TFN-NF membranes, the membrane samples (without support polyester fabric) were fractured in liquid nitrogen into smaller sized strips and sputter coated on the cross-sectional layer with gold-palladium alloy for 100 seconds at a current of 15 mA. The image acquisition was done in secondary electron mode at an acceleration voltage of 20 kV and 1000X magnification.

2.6.4 Topographical characterization of skin surfaces of TFN-NF membranes by AFM

Topographical charaterization of membrane skin surfaces was done by extracting quantitative informations from the three-dimensional (3D) topographies acquired in the semi-contact mode by using an AFM instrument (NT-MDT SOLVER next, Russia). Small squares of approximately 1 cm^2 of the membrane were cut and glued onto a metal substrate. The rectangular cantilever NSG 10 (NT-MDT, Russia) was made out of Si_3N_4 with a spring constant of 11.8 N/m, having a typical resonance frequency of 240 kHz and a nominal tip apex radius of 10 nm with high aspect ratio. The scanning was done on a 10 µm × 10 µm area of the membrane, in air, at room temperature, with a scanning frequency of 0.1 Hz. The scanned regions were flattened using a second order polynomial to remove the curvatures and slopes from the image and then the resulting best fit was subtracted from it. NOVA-P9 software was used for the purpose of image acquisition and evaluation of surface roughness parameters of the membranes. Surface roughness parameters of the membranes were calculated from the height profiles of the image in terms of average roughness (Ra), root mean square roughness (Rq) and ten point height (R_{10Z}).[37]

2.6.5 Elemental analysis and mapping of skin surfaces of TFN-NF membranes

Quantitative surface elemental analysis and mapping were performed by an energy dispersive X-ray spectrometer (EDX) coupled to the SEM and a micro analysis system (INCA Oxford Instruments, UK), employing an accelerating voltage of 20 kV and a magnification of 4000X. It was equipped with an ultrathin beryllium window and 20 mm^2 Si detector. The spectra were acquired for 2 hours to map the elements of interests like N, Zn and O in each membrane. The maximum depth of penetration of

Cite this: DOI: 10.1039/c0xx00000x
www.rsc.org/xxxxxx

the beam (beam diameter: 7.5 nm) inside the sample till its energy of ~10 kV (BE of C-1s: 284.2 eV, BE of O-1s: 543.1 eV, BE of N-1s: 409.9 eV, BE of S-1s: 2472 eV and BE of Zn-1s: 9659 eV) is found (calculated using casino V3, montecarlo simulation of electron trajectory in solids) to be about 3 micron with width of about 3 micron. Thus, the volume of penetration of the e-beam is very small with respect to the large sample volume. The elemental analysis of N, Zn and O, were carried out over 170 points in a grid spectrum where each point was allowed to undergo 60 seconds of detection period.

2.6.6 Cross-flow permeation experiments of TFN-NF membranes

Transport experiments of the Control-NF, Aq-ZnO:TFN-NF and Org-ZnO:TFN-NF class of membranes were conducted in cross-flow test cells, using single feed solutions of three different solutes consisting of varying combination of monovalent and bivalent cations and anions. Solutions of NaCl, $MgCl_2$ and Na_2SO_4, having concentrations iso-osmotic with 0.03 M NaCl were used as feeds. The experiments were conducted at 10 bar transmembrane pressure using a pump with 10 liter per minute feed flow rate. Temperature of the feed solution was maintained at 25 ^oC. Circular membrane samples having an effective membrane area of 15.1 cm^2 were properly washed in deionized water and placed in the test cell with their selective skin layers facing the incoming feed. All the membranes were given sufficient time for stabilization before evaluating of their performances.

The steady state solute rejections of the membranes were determined by measuring the solute concentrations in the feed and permeate using a digital conductivity meter (TESTRONIX 15, Microlab, Mumbai, India). The percent solute rejection, R, was calculated using the expression:

$$R = (1- C_p/C_f) \times 100 \qquad \ldots\ldots\ldots\ldots\ldots\ldots\ldots (1)$$

where, C_p and C_f are the bulk concentrations of the solutes in permeate and feed solutions, respectively. All membrane samples were prepared and tested in duplicate for their NF performances.

The corresponding permeate solvent flux (J_W) was determined by direct measurement of the permeate flow,V (ml), through the membrane of area, A (cm^2), for a given time, t (min), using expression (2) and presented in the units of liter / meter^2 / day (LMD).

$$J_W = V/A.t \quad \ldots\ldots\ldots\ldots\ldots\ldots\ldots\ldots \text{(2)}$$

3 Results and discussion

3.1 Analysis of textural and structural features of nano-ZnO

The X-ray diffraction patterns of nano-ZnO, obtained by thermal decomposition of the acetylacetonate in n-octylamine at 110 ^oC, are shown in Fig. 2. The patterns can be indexed to hexagonal wurtzite lattice structure of the nano-ZnO. The indexing to X-ray patterns is attributed to (100), (002), (101), (102), (110), (103), (200), (112), (201), (004) and (202) peaks of hexagonal crystalline phase of nano-ZnO. The average crystallite sizes as determined using Scherrer's formula ($t = K\lambda/B \cos \theta$, where t = average crystallite size in Å, K = Scherrer constant usually taken as 0.9 Å, λ = X-ray wavelength, θ is the Bragg angle, and B = integral breadth of a reflection located at 2θ) range from 22 ± 2 nm. The lattice structure of the nanocrystals of ZnO can be depicted as a number of alternating planes arranged in tetrahedral and/or octahedral fashion through coordination of O^{2-} and Zn^{2+} ions, stacked alternately along the *c*-axis.

The FTIR spectrum of the as synthesized ZnO nanocrystals, acquired in the atmospheric conditions, is shown in Fig. 3. The most prominent band at 510 cm^{-1} and a weak band at 660 cm^{-1} are assigned to the stretching vibrations of Zn–O bonds, in the tetrahedral and octahedral coordinations, respectively.[38]

Cite this: DOI: 10.1039/c0xx00000x

www.rsc.org/xxxxxx

A Raman spectrum of the ZnO nanocrystals, acquired at room temperature, is shown in Fig. 4. Hexagonal wurtzite structure of ZnO belongs to the space group C_{6v}^4 with two formulae units per primitive cell, where all atoms occupy C_{3v} sites. The Raman active zone-centre optical phonons predicted by group theory is A_1+$2E_2$+E_1. Of these, the phonons of A_1 and E_1 symmetry are polar and both Raman and IR active. Hence, they show different frequencies for the transverse optical (TO) and longitudinal optical (LO) phonons. A weak band at 407 cm^{-1} is assigned to E_1TO phonon mode. The nonpolar optical phonon modes with symmetry E_2, being Raman active only, exhibit dual frequencies where E_2 (Low frequency) at 99 cm^{-1} is associated with oxygen atoms and E_2 (High frequency) at 437 cm^{-1} is associated with the sublattice of Zn, which are characteristic of the wurtzite hexagonal phase of ZnO.[39-42] The XRD, FTIR and Raman scattering measurements confirm the formation of ZnO nanocrystals in hexagonal wurtzite structure.

XPS analysis of the ZnO nanocrystals exhibits presence of a strong peak (Fig. 5a) at 1020.5 eV with FWHM of 2.20 eV, attributed to Zn-$2p_{3/2}$ and a weaker peak at 1043.8 eV with FWHM of 2.21 eV, attributed to Zn-$2p_{1/2}$.[43] In Fig. 5b, the component peaks of the deconvoluted O-1s photoelectron spectrum show the presence of a dominant O-1s peak with lowest binding energy, centered at 529.8 eV with FWHM of 1.79 eV, which can be indexed to the surface and near-surface region lattice oxygen of the hexagonal lattices of nano-ZnO. A distinct higher binding energy of O-1s peak at 531.3 eV, with FWHM of 1.63 eV, can be ascribed to the strongly anchored hydroxyl groups (Zn-OH) at different intrinsic or extrinsic defect sites or oxygen vacancies (O_v) of nano-ZnO.[44] However, the weakest but relatively broadened shoulder peak at 532.5 eV with FWHM of 2.04 eV is due to chemisorbed oxygen contributed by surface hydroxyl groups.[45]

3.2 Characterization of skin layers of TFN-NF membranes by XPS

Representative TFN-NF membranes, one each from the series made by introducing nano-ZnO through aqueous phase as well as organic phase, (i.e. Aq-ZnO:TFN-NF-2 and Org-ZnO:TFN-NF-2) were employed for XPS analysis to investigate the electronic and molecular level interactions of the nanocomposite polyamide skin layers, within the XPS probe depth (5-10 nm). Further, comparisons of XPS analysis of skin layers of these two membranes with that of the Control-NF were made, with respect to the variation in core level binding energies and respective peak areas, to study the effect of nano-ZnO impregnation in polyamide matrices.

The Zn-2p photoelectron spectra of nano-ZnO impregnated polyamide skin layer of Aq-ZnO:TFN-NF-2 and Org-ZnO:TFN-NF-2 are presented in Fig. 6b and 6c, respectively. In case of Aq-ZnO:TFN-NF-2, the high intensity peak at low BE of 1020.7 eV (FWHM: 1.87 eV) corresponds to Zn-2p$_{3/2}$ and the peak at higher BE with lower intensity, attributed to Zn-2p$_{1/2}$, appears at 1044 eV (FWHM: 3.64 eV), (Table 1). Similarly, for the Zn-2p photoelectron spectrum of Org-ZnO:TFN-NF-2, the peak corresponding to Zn-2p$_{3/2}$ appears at 1020.6 eV (FWHM: 2.75 eV) and a weaker peak, corresponding to Zn-2p$_{1/2}$, appears at 1043.7 eV (FWHM: 3.94 eV). The value of the fitting parameter, χ^2 reside in the range of 1.12 - 2.25, which validate the fact of proper fitting of the curves in the Zn-2p XPS spectra. No significant deviations in BE values for Zn-2p$_{3/2}$ as well as Zn-2p$_{1/2}$ of both Aq-ZnO:TFN-NF-2 and Org-ZnO:TFN-NF-2, from the corresponding BE values of the pure nano-ZnO, indicate that there is no redistribution of charge density in Zn-O framework and hence, there is no occurence of inter-atomic charge transfer between the nano-ZnO and the host polymeric material. In other words, ZnO does not form any chemical bonds with the host polymer matrix during the nanocomposite polymer formation. Thus, it is assumed that only the peripheral hydroxyl groups of nano-ZnO play a role in forming noncovalent type secondary chemical interactions with the polyamide network. However, a decrease in BE accompanied by broadening of peaks for Zn-2p$_{3/2}$ by 0.88 eV and Zn-2p$_{1/2}$ by 0.30 eV, from Aq-

Cite this: DOI: 10.1039/c0xx00000x

www.rsc.org/xxxxxx

ZnO:TFN-NF-2 to Org-ZnO:TFN-NF-2 are attributed to the presence of clusters of nano-ZnO with a broad size distribution in the skin surface of the later membrane, as compared to the former, where the size distribution is much more uniform.[46-48]

Fig. 6a, 6b and 6c show the O-1s core level photoelectron spectra of skin layer polymers for Control-NF, Aq-ZnO:TFN-NF-2 and Org-ZnO:TFN-NF-2, respectively. The curve fitting and deconvolution of each O-1s XPS spectrum yield two constituent spectra which indicate the presence of oxygen in two different chemical states. The value of χ^2 stay in a range of 1.00 - 1.45 which confirm the fact of proper fitting of the O-1s curves in all the spectra.The intense peak with low BE value of 530.4 eV (FWHM: 1.99 eV) for Control-NF is assigned to physisorbed oxygen (Table 1). The shifting of values to higher BE of 530.9 eV, with concurrent broadening of peaks for both Aq-ZnO:TFN-NF-2 (FWHM: 2.37 eV) and Org-ZnO:TFN-NF-2 (FWHM: 2.36 eV), refer to the collective contribution of physisorbed oxygen as well as the surface and near-surface region lattice oxygen of the impregnated nano-ZnO. The less intense component shoulder peak of the deconvoluted O-1s spectra with higher BE value of 531.9 eV for Control-NF is assigned to oxygen in the structure of C=O of amide linkages of polyamide network[49] and those of Aq-ZnO:TFN-NF-2 (BE: 532.8 eV) and Org-ZnO:TFN-NF-2 (BE: 532.7 eV) are contributions from oxygen in the structure of C=O of amide linkages of polyamide network and surface hydroxyl groups of nano-ZnO. The chemical shifts of 0.9 and 0.8 eV for Aq-ZnO:TFN-NF-2 and Org-ZnO:TFN-NF-2 as compared to Control-NF are ascribed to the chemisorbed surface hydroxyl groups of nano-ZnO. Presence of nano-ZnO leads to an increase in areas for the major peaks by 9.7 and 14.84 % for the Aq-ZnO:TFN-NF-2 and Org-ZnO:TFN-NF-2, respectively over the Control-NF.

The relative area is subsequently compensated in the shoulder peak, which is contribution of amide oxygen and chemisorbed surface hydroxyl groups of the impregnated nano-ZnO.

The component peaks of N-1s spectra (Fig. 6a, 6b and 6c*)* with the high intensity, at lower BE of 398.9, 399.0 and 399.2 eV, for Control-NF, Aq-ZnO:TFN-NF-2 and Org-ZnO:TFN-NF-2, respectively (Table 1), correspond to the 2^o nitrogen atoms of free N-H of polyamides and free 1^o as well as 2^o amines of the polymer backbone. For N-1s XPS spectra, the value of χ^2 reside in the range of 0.90 - 1.75. The peaks with lower intensity at higher BE of 400.6 eV for Control-NF, 400.0 eV for Aq-ZnO:TFN-NF-2 and 400.7 eV for Org-ZnO:TFN-NF-2 are due to 3^o nitrogen atoms of amides and amines of the polymer backbone as well as nitrogen atoms of amines and amides which are involved in intermolecular hydrogen bonding either through inter-chain interaction or through the surface hydroxyl groups of nano-ZnO. The peak positions are concordant with the reported data in literature.[50] A chemical shift of the N-1s signal to higher BE values in case of Control-NF as well as Org-ZnO:TFN-NF-2, as compared to Aq-ZnO:TFN-NF-2, are attributed to enhanced protonation of amine sites, during the course of polycondensation reaction, of the former two membranes. This may result in an increase in the positive charge densities on N sites of these membranes. Peak area referring to free N-H sites in the polyamide, corresponding to the Control-NF, decreases by 14.02 % as nano-ZnO of 0.1 % is incorporated in the skin surface of Aq-ZnO:TFN-NF-2. This is ascribed to the extensive association of the nano-ZnO with N-H of polyamides and 1^o as well as 2^o amines of polymer backbone, reducing the number of free amine sites. However, the peak area assigned to such N-H sites corresponding to the Org-ZnO:TFN-NF-2 increases only by 2.56 % as compared to the Control-NF indicating that there are less extensive H bondings and existence of more free N-H sites. These changes in the areas of the major peaks for Aq-ZnO:TFN-NF-2 and Org-ZnO:TFN-NF-2 are compensated in the areas of the shoulder peaks at higher BE. The peak areas of N and O are sensitive to the presence and variation of nano-ZnO in the polyamide skin layer, and hence may not be considered as absolute.

Journal Name

Dynamic Article Links ►

Cite this: DOI: 10.1039/c0xx00000x

www.rsc.org/xxxxxx

ARTICLE TYPE

3.3 Spectral characterization of TFN-NF membranes by ATR FTIR

ATR FTIR spectrum of Control-NF and those of the TFN-NF membranes, made by introducing nano-ZnO either through aqueous or organic phase, are presented in Fig. 7a and 7b, respectively. They show that introduction of progressively increasing amounts of nano-ZnO through either medium leads to significant physicochemical changes in the skin layer polymers of the resulting nanocomposite membranes.

The ZnO nanoparticles, produced by synthesis in n-octylamine as in the present case, is known to have a tendency to chemisorb water molecules on its surface making it predominantly hydrophilic[51,52] and assuming a structure where the core material is enveloped in a sheath of hydroxyl groups. When this nano-ZnO, at varying concentration of 0.05, 0.1 and 0.2 (w/v) %, is taken in the aqueous monomeric solution containing PEI, due to the alkaline nature of the solution, it remains in the form of nano-$ZnO(OH)_n$, where ‘n’ represents the number of surface anchored hydroxyl groups depending on pH of the medium.[53] In this phase, extensive noncovalent type secondary chemical interactions occur, mostly in the form of H-bondings, between surface hydroxyl groups of nano-ZnO and the amine groups of the branched PEI monomer. These H-bondings preferentially engage the primary amine sites of PEI, because, in addition to being more electropositive than the H of the secondary amines, the former sites are known to be oriented more towards outside in a somewhat spherically coiled structure of the polymer.[54] When PEI, in the form of this molecular association, participates in interfacial polycondensation reaction with TMC, the resulting crosslinked polyamide is assumed to form similar H-bondings involving peripheral OH of nano-ZnO and N-H as well as >C=O of amide groups of the polyamide. Thus, when nano-ZnO accommodates in the interstices of the nanocomposite polymer it promotes more H-bondings in the polyamide network structure of Aq-ZnO:TFN-NF-1 than that of the Control-NF. The ATR FTIR spectra of the nanocomposite membranes, presented in Fig. 7a, corroborate these facts where deviations are seen in both amide-I region i.e. in carbonyl stretching frequency, $\nu_{C=O}$ and amide-A region i.e. N-H stretching frequency, ν_{N-H} of the Aq-ZnO:TFN-NF-1 from those of the Control-NF. Thus, with incorporation of 0.05 % nano-ZnO in Aq-ZnO:TFN-NF-1, the $\nu_{C=O}$ value show a red shift from 1656 to 1647 cm^{-1} and ν_{N-H} from 3268 to 3264 cm^{-1}. However, a reverse trend is noticed, showing a blue shift for $\nu_{C=O}$ from 1647 to 1661 cm^{-1} and then to 1664 cm^{-1} as well as for ν_{N-H}, from 3264 to 3279 cm^{-1} and further to 3288 cm^{-1}, with incremental addition of 0.1 and 0.2 % nano-ZnO in making the respective membranes. This reversal of trend is assumed to happen because, at this higher concentration the nanomaterials find much less space to accommodate in the resulting polymer network, forcing a reorganization of the polymer chains and subsequent disruption of the intermolecular H-bondings. The blue shift in $\nu_{C=O}$ values may further reflect the fact that with enhanced nanoparticle density in the nanocomposite polymer matrix there is a decline of dipole-dipole interaction or $n \rightarrow \pi^*$ interaction happening though delocalization of a lone pair (n) of the donor carbonyl groups of amide segments or amine groups of the PEI chains into the antibonding (π^*) orbital of the acceptor carbonyl groups (C=O·····C=O or C-N·····C=O) of the adjacent polymer chains. This also supports the above mentioned occurrence of reorganization of the polymer chains, affecting the conformationally sensitive amide-I region of amide segments.[55-57]

In contrast to the aqueous phase, introduction of nano-ZnO in the polyamide matrix through the organic phase results in an initial blue shift in the $\nu_{C=O}$ from 1656 to 1663 cm^{-1} and ν_{N-H} from 3268 to 3285 cm^{-1}, for Org-ZnO:TFN-NF-1 as compared to the Control-NF (Fig. 7b). It is well known that there are extensive intermolecular H-bondings between the amide-I and amide-A regions as well as strong dipole-dipole interaction or $n \rightarrow \pi^*$ interaction among the adjacent chains of polyamides of Control-NF. More number of conformationally free >C=O groups in Org-ZnO:TFN-NF-1, evident

Cite this: DOI: 10.1039/c0xx00000x

www.rsc.org/xxxxxx

from its higher $\nu_{C=O}$ value, than the Control-NF, implies that there is less extensive H-bondings in the nanocomposite polymer matrix. This is possible if the polymer chains of the former membrane are further away from each other, with less number of >C=O groups present within the range of H-bonding distance with the adjacent H atom of either N-H of the amide group or peripheral OH of ZnO, to experience extensive noncovalent interactions. The pathway of nonpolar organic medium, employed for introduction of nano-ZnO, may be responsible for this type of network structure of the nanocomposite polyamide, resulting in lesser extent of H-bondings for Org-ZnO:TFN-NF-1. This is in contrast with the counterpart of aqueous phase i.e. Aq-ZnO:TFN-NF-1. However, with increase in nanoparticle density in the organic phase from 0.05 to 0.1 and then to 0.2 (w/v) %, a red shift occurs from 1663 to 1656 cm^{-1} via 1658 cm^{-1} for $\nu_{C=O}$ and 3285 to 3260 cm^{-1} through 3274 cm^{-1} for ν_{N-H}. The former change can be ascribed to an increase in secondary chemical interactions within the nanocomposite polyamide matrix which is assumed to happen because of distribution of more nano-ZnO in the open interstices of the polyamide network promoting more H-bondings between the surface OH of the nano-ZnO and the nearby >C=O groups of the polyamide. However, the later change, in ν_{N-H}, may result mostly due to the involvement of more NH sites in forming association with the liberated HCl during the course of reaction which can further lead to progressive increase in positive charge densities of the membranes. The ATR FT IR results of both classes of membranes show that the medium of incorporating nanomaterial into TFN-NF membranes has significant influence over the nature of interaction within the polymer network and physicochemical features of the inorganic-polymer hybrid material.

3.4 Analysis of skin surface morphology of TFN-NF membranes by SEM

The compatibility of nano-ZnO as a constituent of the monomeric aqueous amine phase is evident from a clear homogenous nano-ZnO/PEI/water solution (Fig. 8b). In contrast, the turbid suspensions of nano-ZnO/water solution (Fig. 8a) and of nano-ZnO/TMC/n-hexane solution (Fig. 8c) indicate the physicochemical incompatibility of the nanomaterials in the medium. Electrodynamic interactions between the nano-ZnO and the two respective dispersion media, water and n-hexane, play significant roles in determining the interparticle interactions. Thus, van der Waals pair interaction energy which is proportionally dependent on a material dependent property, Hamaker constant that varies with the contrast between the dielectric constants of nanoparticles and the dispersion medium, and inversely dependent on the separation distance between the particles that differs with the concentration and surrounding chemical environment of the particle, becomes a measure of stability for such dispersions. Higher value of Hamaker constant for nano-ZnO in water (26×10^{-21} J) as compared to that in n-hexane (19×10^{-21} J) reflects the higher degree of incompatibility of nano-ZnO in water than in n-hexane since a higher value of the parameter implies greater interparticle attractive force and, hence, more prone is the system to come closer and induce flocculation.[58] However, in the PEI environment of the aqueous monomeric solution the flocculation of nano-ZnO gets restricted due to a reduction in the attractive van der Waals inter-particle potential through accumulation of PEI chains on their surfaces. The steric repulsion between the chains of branched PEI molecules on the exterior of sheathed nano-ZnO also helps in stabilization of the solution, emphasizing the role of the former in enhancing the physicochemical compatibility of the later in the solution.[59]

Scanning electron micrographs of skin layer as well as cross-sections of the Aq-ZnO:TFN-NF class of membranes are presented in Fig. 9a, 9b and 9c. Skin layer images show that the particles of nano-ZnO are well accommodated and evenly distributed inside the nanocomposite polyamide matrix of the membrane, formed through interfacial polycondensation process. With increase in concentration of the

Cite this: DOI: 10.1039/c0xx00000x
www.rsc.org/xxxxxx

nano-ZnO from 0.05 to 0.2 %, their density on the skin layer of the membranes is seen to increase, which is supposed to perturb the polymeric chains through stretching and induce deformation in the network structure. As the nano-ZnO domains grow with increase of concentration, they are seen to arrange themselves forming some long range ordering and patterns indicating that there is a cohesive interaction between the nanomaterials themselves as well as between the nanomaterials and the polymer chains. This pattern formation presumably occurs through multiple-point secondary chemical interactions between the nano-ZnO and the polyamide network which leads to a significant loss of translational entropy for the particles as well as conformational entropy for the polymeric chains. At higher nano-ZnO density of 0.2 %, therefore, there is formation of more number of smaller coils of the nanomaterials in the polymer matrix to compensate the entropy loss.[60]

In contrast to the aqueous amine medium, the nano-ZnO is chemically incompatible in solution of n-hexane containing TMC and results in the formation of an unstable dispersion (Fig. 8c). The skin surface as well as cross-sectional SEM images of the Org-ZnO:TFN-NF class of membranes, prepared by introduction of nano-ZnO via organic phase, presented in Fig. 10a, 10b and 10c. Skin layer images show that the nanomaterials are not evenly distributed in the polymer matrix but rather present in the form of discrete clusters whose number and size increase with increasing concentration of the nanomaterials in the organic phase. This indicates that the nanomaterials are unable to cohesively accommodate themselves within the polymer matrix when they are introduced through the organic phase. The orders and patterns found in the membranes of the Aq-ZnO:TFN-NF series are significantly missing. Since, formation of the thin skin layer of the TFN-NF membrane, takes place through crossing over of the PEI monomers from the aqueous phase to the organic side, across the polymer barrier (Fig. 1b), in a diffusion controlled manner by *in-situ* interfacial polycondensation route,[61] the nanomaterials do not get enough chance of encountering a compatible polar environment to get evenly distributed, before being embedded in the polyamide matrix. This results in an uneven distribution of the nano-ZnO in the form of uneven clusters in the resultant polyamide network.

These observations through SEM studies emphasize the fact that the dynamics of skin layer formation through interfacial polycondensation process, distribution of the nanomaterials within the skin layer and the resultant skin layer morphology of the nano-ZnO impregnated TFN-NF membranes are influenced by the type of precursor media employed for dispersion of the nano-ZnO to a great extent.

3.5 Evaluation of skin surface topographies of the TFN-NF membranes by AFM

The 3D AFM images as well as the respective height histograms of TFN-NF membranes, prepared by introducing nano-ZnO through aqueous phase are presented in Fig. 11. They show that the surface topographies of the membranes change significantly, from a relatively smooth profile for the membrane Aq-ZnO:TFN-NF-1 to progressively rougher surfaces for membranes made with impregnation of more and more nanomaterials. Further, formations of patterns on the surfaces of membranes, a feature observed in the respective SEM images as well, justify the occurrence of long range association of the nanomaterials in the polymer matrix. The 3D AFM images of Aq-ZnO:TFN-NF class of membranes, read along with the corresponding height histograms, show that the peaks are more or less uniform in height, having a very narrow distribution between 18 to 28 nm for Aq-ZnO:TFN-NF-1, however, in case of Aq-ZnO:TFN-NF-2, the surface is seen to be populated with a larger number of peaks, whose heights are significantly more than those of Aq-ZnO:TFN-NF-1, most of them occurring between 20 to 130 nm, contributing to a much broader distribution pattern. The higher area of the height histogram of Aq-ZnO:TFN-NF-2 also indicates a higher peakedness of this membrane compared to Aq-ZnO:TFN-NF-1 and consequently, an increased membrane surface area of

Cite this: DOI: 10.1039/c0xx00000x

www.rsc.org/xxxxxx

ARTICLE TYPE

the former membrane than the latter. With a still higher concentration of the nanomaterial, in Aq-ZnO:TFN-NF-3, the peak heights of the membrane are far from uniform, their distribution is much wider and range between 10 to 270 nm. A significant tail in the height histogram suggests the presence of a few isolated high peaks with heights between 150 to 270 nm. As compared to Aq-ZnO:TFN-NF-2, where a number of narrow peaks are distributed over the entire surface of the membrane, the presence of higher concentration of nano-ZnO makes some of the isolated high peaks in Aq-ZnO:TFN-NF-3 quite broad.

The computed amplitude parameters of the nanocomposite membranes, presented in Table 2, shows that the average roughness (R_a) of the membranes increase from 1.48 to 17.59 nm and further to 31.69 nm as concentration of nanomaterials in the aqueous monomer solution are increased. The corresponding root mean square roughness (R_q) of the membrane increases from 2.09 to 21.96 nm and finally to 41.96 nm. This is in accordance with the topographical features discussed in response to their 3D images. R_{10z}, which is the difference in heights between the average of the five highest peaks and the five lowest valleys relative to the mean plane, denotes the contrast between the heights and depths of extreme peaks and valleys that may be occasionally present on the surface of the membrane. The lowest R_{10z} value of 9.96 nm for Aq-ZnO:TFN-NF-1 results from a surface having peaks and valleys of less contrast in heights and depths. However, impregnation of still higher amount of nanomaterials lead to higher values of R_{10z} for Aq-ZnO:TFN-NF-2 (39.89 nm) and Aq-ZnO:TFN-NF-3 (101.57 nm) which indicate the occurrence of more contrast in heights and depths due to the onset of formation of isolated high peaks and low valleys on the membrane surface.

The 3D AFM images and height histograms of the Org-ZnO:TFN-NF class of membranes, prepared by introduction of nano-ZnO through organic phase, presented in Fig. 12, show different type of surface topographies than the membranes prepared by introduction of the nanomaterials through the aqueous phase. The occurrence of long range patterns due to distribution of nano-ZnO in the polymer nanocomposite, a characteristic of the latter class of membranes, are significantly absent. The nanomaterials, though found present throughout the skin surface of the membranes in the form of discrete clusters, are not evenly distributed. The 3D images and the respective height histograms for Org-ZnO:TFN-NF-1 and Org-ZnO:TFN-NF-2 show that the number of peaks are fewer and their heights are much smaller than the respective membranes of aqueous phase. For the Org-ZnO:TFN-NF-1, the peak heights on the membrane surface are between 20 to 45 nm and, for Org-ZnO:TFN-NF-2, they are between 10 to 45 nm. However, for Org-ZnO:TFN-NF-3, the peak heights range between 100 to 500 nm which is due to the presence of occasional high peaks on the surface of the membrane caused by entrapment of larger sized clusters of nano-ZnO in the polyamide network.

The R_a values of the membranes, listed in Table 2, show that they are 4.07 and 5.58 nm when 0.05 and 0.1% of the nano-ZnO were used. This nominal increase in the roughness values is due to the absence of any significant number of peaks on the membrane surface, unlike their counterparts of the aqueous phase membranes. However, the R_a value increases to 49.09 nm in the membrane, Org-ZnO:TFN-NF-3 which is believed to be due to the uneven distribution of the entrapped clusters of nanomaterials in the polymer matrix of the membrane. The variation in surface topography, due to the effect of impregnation of nano-ZnO at progressively higher concentrations is also manifested through the change of R_q and R_{10z} values.

Cite this: DOI: 10.1039/c0xx00000x

www.rsc.org/xxxxxx

ARTICLE TYPE

The AFM studies bring out the fact that surface roughness features such as formation, distribution as well as variation of peaks and valleys are highly influenced by the nature of the medium through which nanomaterials are impregnated into the skin layer of TFN-NF membranes.

3.6 Elemental analysis and mapping of TFN-NF membranes by EDX

The skin layer elemental mappings of both Aq-ZnO:TFN-NF and Org-ZnO:TFN-NF class of membranes presented in Fig. 13 and Fig. 14, respectively, show a differential distribution of the elements (N, Zn and O) within the bulk of skin layer, with increasing amount of nanomaterial impregnation. Elemental analysis of the Aq-ZnO:TFN-NF class of membranes by EDX, presented in Table 3 reveals that when the nano-ZnO concentration is increased from 0.05 to 0.1 % and then to 0.2 %, the relative nanoparticle density in the skin layer polyamide matrix increases from 2.48 ± 0.12 weight % (i.e. 0.64 atomic %) to 7.33 ± 0.13 weight % (1.83 atomic %) and finally to 10.02 ± 0.29 weight % (3.65 atomic %). The corresponding values of relative atomic ratios of the unique elements Zn and N (i.e., Zn:N) in the skin layers of these membranes show an increasing trend from 1:44.02 to 1:7.24 through 1:15.04.

However, increase in the respective values of the Org-ZnO:TFN-NF class of membranes are much higher. The nano-ZnO density increases from 3.05 ± 0.59 weight % (0.82 atomic %) to 9.16 ± 0.20 weight % (2.33 atomic %) and then to as high as 16.57 ± 0.29 weight % (4.40 atomic %) with introduction of 0.05, 0.1 and 0.2% of nano-ZnO, respectively. Similarly, the relative atomic ratios of the unique elements Zn and N of these membranes increase from 1:34.21 to 1:11.69 and finally to 1:5.93 indicating incorporation of progressively more amount of nano-ZnO in the nanocomposite polyamide skin layer. The determined elemental ratios of the unique elements do not refer only about the composition of the skin layer (~ 500 nm), but also imply the contribution of these elements residing underneath the polyamide layer i.e., polysulfone layer (~ 3 μm).

Impregnations of higher amount of nano-ZnO in skin layer of the latter class of the membranes have also been observed during their respective SEM and AFM analyses. This happens so because, during the progress of heterogeneous type interfacial polycondensation reaction and successive formation of nascent polymer layer, the migrating reactant PEI meets the reactant of the organic phase i.e. TMC (with or without nano-ZnO, as the case may be), in the organic phase (Fig. 1) close to the boundary between the mutually immiscible solvents. In this situation, when the nanomaterials are present in the organic phase, there is a possibility of more nano-ZnO being present in the reaction zone during the process of polycondensation reaction. The unstable dispersion of the nanomaterial in the organic medium may further be responsible for some deposition and subsequent entrapment of the nano-ZnO in the skin layer of the membrane. But, when the nano-ZnO becomes a constituent of the aqueous amine phase, the monomer along with nano-ZnO has to cross the barrier of the nascent polyamide film and approach the reactants of the organic phase to undergo further polymerization. The transport of nano-ZnO in the reaction zone may not be facilitated since, the rate of diffusion across the nascent polymeric barrier, for the bulky sized nano-ZnO associated constituent PEI of the aqueous amine phase, becomes comparatively slow. This may be responsible for presence of less amount of nano-ZnO in the skin layer polyamide of Aq-ZnO:TFN class of membranes.

3.7 Evaluation of transport characteristics of TFN-NF membranes

The solute rejection behaviors of the Aq-ZnO:TFN-NF class of membranes as welll as that of the Control-NF, presented in Fig. 15a, show that the TFN-NF membranes give much higher rejections for $MgCl_2$ than for NaCl and Na_2SO_4, which follows a general trend $MgCl_2 > NaCl \geq Na_2SO_4$. This

Cite this: DOI: 10.1039/c0xx00000x
www.rsc.org/xxxxxx

implies that the membranes are inherently positively charged which is characteristic of membranes derived using PEI. It is observed that with increase in concentration of nano-ZnO in the skin layers of the membranes there is a decline in the differential rejection between these three solutes, more specifically between $MgCl_2$ and Na_2SO_4. Their solute rejection ratios of 92.3:51.3, 87.6:50.2 and 84.2:48.4 indicate the possibility of decrease in the surface positive charge of the membranes with enhanced incorporation of nano-ZnO in the nanocomposite matrix. However, this may not be the sole factor for this trend since morphological factors, especially the possibility of formation of a more open polymer matrix further influences the porous nature of the nanocomposite membranes, consequently contributing to an overall decline of SR values for all the solutes. In these positively charged membranes, the maximum solute rejection for $MgCl_2$ is predominantly governed by Donnan exclusion, where, due to presence of the multivalent cation (Mg^{2+}) with higher positive charge density, the solute experiences maximum electrostatic repulsion by the charged membranes.[62-64] A lower solute rejection of NaCl is due to a poorer Donnan exclusion of the monovalent Na^+ ions by the membrane. However, the presence of bivalent anion in Na_2SO_4 facilitates its transport through the membrane further lowering the respective solute rejection.

A similar order of solute rejection pattern, $MgCl_2 > NaCl \geq Na_2SO_4$, for Org-ZnO:TFN-NF class of membranes, however comes with a superior differential rejection ability between $MgCl_2$ and Na_2SO_4, as compared to the Aq-ZnO:TFN-NF class of membranes (Fig. 15b). This signifies a higher positive charge of the Org-ZnO:TFN-NF class of membranes, the origin of which has been discussed during characterization of the skin layers of the membranes by FTIR as well as XPS. Consequently, the solute rejection ratios for $MgCl_2$ and Na_2SO_4 of the Org-ZnO:TFN-NF-1, Org-ZnO:TFN-NF-2 and Org-

ZnO:TFN-NF-3 show an increasing trend i.e. 92.3:46.4, 91.6:43.6 and 90.3:41.2, respectively. However, decline in the solute rejections of Org-ZnO:TFN-NF class of membranes, with increase in concentration of nano-ZnO beyond 0.05 %, is not as pronounced as the Aq-ZnO:TFN-NF class of membranes.

Both the classes of TFN-NF membranes show significant increase in their solvent fluxes, with progressive impregnation of nano-ZnO in making the membranes. Solvent fluxes for the representative solute $MgCl_2$ increase from 520 LMD for Control-NF to 600 LMD for Aq-ZnO:TFN-NF-1, 960 LMD for Aq-ZnO:TFN-NF-2 and 920 LMD for Aq-ZnO:TFN-NF-3 (Fig.16a). Similarly, the solvent fluxes increase from 520 LMD for Control-NF to 560 LMD for Org-ZnO:TFN-NF-1, 620 LMD for Org-ZnO:TFN-NF-2 and finally to 660 LMD for Org-ZnO:TFN-NF-3 (Fig.16b). The increase of solvent fluxes in TFN class of membranes has been widely reported in litereature, where the improvement is attributed to the presence of nanomaterials in the interfacial reaction zone, influencing the kinetics of interfacial polycondensation reaction by factors like change in miscibility of the aqueous and organic phases through release of heat of hydration of nanomaterials, change in diffusion rate of monomers which consequently alter the cross-linking density of the polymer network and hydrophilic/hydrophobic nature of the membrane surfaces.[65-67]

For Org-ZnO:TFN-NF class of membranes, the free PEI molecules (since it is devoid of the nano-ZnO) experience a better mobility and diffusivity to migrate from aqueous to the organic phase, across the nascent polymer layer, ensuring an enhanced rate of polymerization in the reaction zone. Also, the heat of hydration of nano-ZnO, which are present in considerable density in the organic phase, could induce an increase of local temperature in the reaction zone as the nanoparticles encounter the hydrated PEI molecules. This thermal impact can additionally contribute to improve the miscibility of the two heterogeneous phases locally and subsequently facilitate the reaction by enhancing the rate of diffusion

Cite this: DOI: 10.1039/c0xx00000x

www.rsc.org/xxxxxx

ARTICLE TYPE

of the PEI monomers into the organic phase.[65] But, such thermal effect may have some influence in the exothermic type polycondensation reaction to reduce the reactivity. Thus, it can be assumed that impregnation of more nano-ZnO tune the reaction in such a manner that it becomes kinetically more favourable, though thermodynamically adverse. However, the overall effect results in formation of a skin layer with a cross-linked polymer network with an enhanced solvent permeability. Simultaneously, as evident from the morphological and topographical analyses, the nanomaterials are less uniformly distributed in the skin layer matrix of the membrane, forming rather discrete clusters, due to an unstable dispersion of nanomaterials in the organic monomeric phase (Fig. 8c). These factors lead to a nanocomposite polymer layer where the clusters of nano-ZnO might block some entrances of the channels for solvent flow in the membranes, resulting in a lesser extent of increase of the solvent fluxes of the Org-ZnO:TFN-NF class of membranes as compared to the Aq-ZnO:TFN-NF class of membranes.[68,69]

In the case of Aq-ZnO:TFN-NF class of membranes, bulky nature of the nano-ZnO associated PEI molecules in the aqueous phase leads to restricted mobility and slow rate of diffusion of the monomer from aqueous to the organic phase across the nascent interfacial polymer layer resulting in a reduced reactivity which may result in kinetic inhibition in the growth of the polymer film. Further, an open structure in the polymer network as described in SEM analysis and a probable increase in membranes' pore sizes - reflected in the reduced solute rejection - make the flow of solvent easier.[70,71] The significant peakedness of the membrane, observed in their AFM images, due to nanomaterial incorporation, is supposed to increase the effective surface area of the membranes. These factors collectively account for the increase of solvent fluxes of these membranes prepared by introducing nano-ZnO through aqueous phase. However, a reduced solute rejection with no accompanying increase in solvent flux for the Aq-ZnO:TFN-NF-3 indicates that the increased concentration of the nano-ZnO at this level may be acting as pore blocker residing within the channels of solvent flow, hindering the flow of the solvent through this membrane, and, at the same time, introducing some defects in the skin layer of the membrane lowering its solute rejection ability.

4 Conclusions

TFN-NF membranes with nano-ZnO impregnated polyamide matrices have been prepared following different routes of impregnation of the nanomaterial during *in-situ* interfacial polymerization of reactive monomers. Effects of variation of route specific introduction of nano-ZnO into the skin layer polymer matrix through either aqueous or organic phase route, have been evaluated extensively by instrumental techniques. Structural characterizations by XPS and ATR FTIR have probed the interactions of the nano-ZnO and its coexistence in the hybrid nanocomposite material. Morphological and topographical characterizations by SEM and AFM revealed that adoption of these routes yielded membranes with distinctly different surface features. The uniformity in distribution of the nano-ZnO was less in the skin surface of Org-ZnO:TFN-NF membranes than when they were introduced through the aqueous phase. The distinctly positively charged membranes provided differential solute rejections for solutes having varying combinations of cations and anions in the order of $MgCl_2 > NaCl \geq Na_2SO_4$. Introduction of nano-ZnO improved the solvent fluxes of the membranes significantly, particularly in the Aq-ZnO:TFN-NF set of membranes. The paper has attempted to establish correlations between the factors leading to dynamic membrane formation and the resulting physicochemical features as well as transport properties.

Cite this: DOI: 10.1039/c0xx00000x

www.rsc.org/xxxxxx

ARTICLE TYPE

Notes and references

1 Mulder, M. Basic Principles of Membrane Technology, 2nd ed.; Kluwer Academic Publishers: Netherlands, 1998.

2 R. J. Peterson, *J. Membr. Sci.,* 1993, **83**, 81–150.

3 A. E. Childress, M. Elimelech, *J. Membr. Sci.,* 1996, **119,** 253-268.

4 D. X. Wang, M. Su, Z. Y. Yu, X. L. Wang, M. Ando, Takuji Shintani, *Desalination*, 2005, **175,** 219-225.

5 B. Al-Rashdi, C. Somerfield, N. Hilal, *Sep. Purif. Rev.*, 2011, **40,** 209-259.

6 B. Balannec, M. Yourch, M. R. Baudry, B. Chayfer, *Sep. Purif. Technol.*, 2005, **42,** 195–200.

7 J. Radjenovic, M. Petrovic, F. Ventura, D. Barcelo, *Water Research*, 2008, **42,** 3601 – 3610.

8 N. Capelle, P. Moulin, F. Charbit, R. Gallo, *J. Membr. Sci.*, 2002, **196**, 125–141.

9 C. Tang, V. Chen, *Desalination*, 2002, **143,** 11-20.

10 S. J. Sarrade, G. M. Rios, M. Carle`s, *Sep. Purif. Technol.*, 1998, **14,** 19–25.

11 B. H. Jeong, E. M. V. Hoek, Y. Yan, A. Huang, X. Subramani, G. Hurwitz, A. K. Ghosh, A. Jawor, *J. Membr. Sci.*, 2007, **294,** 1–7.

12 S. Y. Kwa, S. H. Kim, *Environ. Sci. Technol.*, 2001, **35,** 2388–239.

13 S. Sorribas, P. Gorgojo, C. Téllez, J. Coronas, A. G. Li, *J. Am. Chem. Soc.*, 2013, **40**, 15201–15208.

14 M. G. Buonomenna, *Desalination*, 2013, **314,** 73–88.

15 J. Shen, H. Ruan, L. Wu, C. Gao, *Chemical Engineering Journal*, 2011, **168,** 1272–1278.

16 J. Huang, K. Zhang, K. Wang, Z. Xie, B. Ladewig, H. Wang, *J. Membr. Sci.*, 2012, **423–424**, 362–370.

17 N. Maximous, G. Nakhla, W. Wan, K. Wong, *J. Membr. Sci.*, 2009, **341**, 67–75.

18 N. Maximous, G. Nakhla, K. Wong, W. Wan, *Sep. Purif. Technol.*, 2010, **73,** 294–301.

19 H. S. Lee, S. J. Im, J. H. Kim, H. J. Kim, J. P. Kim, B. R. Min, *Desalination*, 2008, **219,** 48-56.

20 Y. Mansourpanah, S. S. Madaeni, A. Rahimpour, A. Farhadian, A. H. Taheri, *J. Membr. Sci.*, 2009, **330**, 297-306.

21 J. H. Li, Y. Y. Xu, L. P. Zhu, J. H. Wang, C. H. Du, *J. Membr. Sci.*, 2009, **326**, 659-666.

22 M. Sairam, B.V. K. Naidu, S. K. Nataraj, B. Sreedhar, T. M. Aminabhavi, *J. Membr. Sci.*, 2006, **283**, 65–73.

23 C. P. Leo, W. P. C. Lee, A. L. Ahmad, A. W. Mohammad, *Sep. Purif. Technol.*, 2012, **89**, 51–56.

24 L. Shen, X. Bian, X. Lu, L. Shi, Z. Liu, L. Chen, Z. Hou, K. Fan, *Desalination*, 2012, **293**, 21–29.

25 M. L. Lind, D. E. Suk, T. V. Nguyen, E. M. V. Hoek, *Environ. Sci. Technol.*, 2010, **44**, 8230–8235.

26 M. L. Lind, A. K. Ghosh, A. Jawor, X. Huang, W. Hou, Y. Yang, E. M. V. Hoek, *Langmuir*, 2009, **25,** 10139–10145.

27 Z. Emami-Karvani, P. Chehrazi, *Afr. J. Microbiol. Res.*, 2011, **5**, 1368-1373.

28 J. Sawai, *J. Microbiol. Methods*, 2003, **54**, 177–182.

29 M. Yan, Y. Song, C. P. Wong, K. Hardin, E. Ho, *The Journal of Nutrition*, 2008, **138**, 667-673.

30 L. K. Adams, D. Y. Lyon, P. J. J. Alvarez, *Water Research*, 2006, **40**, 3527–3532.

31 R. Brayner, R. Ferrari-Iliou, N. Brivois, S. Djediat, M. F. Benedetti, F. Fiévet, *Nano Lett.*, 2006, **6**, 866–870.

32 H. A. Jeng, J. Swanson, J. Environ. Sci. Health, Part A: Toxic/Hazard. Subst. Environ. Eng., 2006, **41**, 2699–2711.

33 K. R. Raghupathi, R. T. Koodali, A. C. Manna, *Langmuir*, 2011, **27,** 4020-4028.

34 N. Jones, B. Ray, K. T. Ranjit, A. C. Manna, *FEMS Microbiol. Lett.*, 2008, **279**, 71–76.

35 J. M. Yousef, E. N. Danial, *Journal of Health Sciences*, 2012, **2**, 38-42.

36 G. Rudolph; M. C. Henry, Inorganic Syntheses, 1967, **10**, 74.

37 E. S. Gadelmawla, M. M. Koura, T. M. A. Maksoud, I. M. Elewa, H. H. Soliman, *J. Mater. Process. Technol.*, 2002, **123**, 133–145.

38 R. Elilarassi, G. Chandrasekaran, *Mater. Chem. Phys.*, 2010, **123**, Issue no. 2–3, 450–455.

39 T. C. Damen, S. P. S. Porto, B. Tell, *Phys. Rev.*, 1966, **142**, 570–574.

40 Y. J. Xing, Z. H. Xi, Z. Q. Xue, X. D. Zhang, J. H. Song, R. M. Wang, J. Xu, Y. Song, S. L. Zhang, D. P. Yu, *Appl. Phys. Lett.*, 2003, **83**, 1689–1691.

41 A. Umar, Y. B. Hahn, *Appl. Phys. Lett.*, 2006, **88**, 173120–173122.

42 I. Calizo, A. K. Alim, V. A. Fonoberov, S. Krishnakumar, M. Shamsa, A. A. Balandin, R. Kurtz, *Proc. of SPIE 2007, 6481, Quantum Dots, Particles, and Nanoclusters IV*, 64810N-1– 64810N-8.

43 A. A. Ashkarran, S. M. Mahdavi, M. M. Ahadian, *Appl. Phys. A: Mater. Sci. Process.*, 2010, **100**, 1097–1102.

44 Z. Li, Y. Xiong, Y. Xie, *Inorganic Chemistry*, 2003, **42**, Issue No. 24, 8105-8109.

45 X. Zhang, J. Qin, Y. Xue, P. Yu, B. Zhang, L. Wang, R. Liu, *Nature Scientific Reports 4*, 2014, Article number: 4596.

46 H. S. Shin, H. C. Choi, Y. Jung, S. B. Kim, H. J. Song, H. J. Shin, *Chem. Phys. Lett.*, 2004, **383**, 418–422.

47 C. N. R. Rao, V. Vijayakrishnan, Aiyer, N. Hemantkumar, G. U. Kulkarni, G. N. Subbanna, *J. Phys. Chem.*, 1993, **97,** 11157-11160.

48 G. K. Wertheim, *Z. Phys. B-Condensed Matter,* 1987, **66**, 53-63.

49 D. H. Shin, N. Kim, Y. T. Lee, *J. Membr. Sci.*, 2011, **376**, 302–311.

50 M. J. Ariza, E. R. Castell´on, R. Rico, J. Benavente, M. Mu˜noz, M. Oleinikova*, J. Colloid Interface Sci.*, 2000, **226**, 151–158.

51 D. Maity, J. Ding, *Int. J. of Nanoscience*, 2011, **10**, 943-947.

52 K. Namratha, M. B. Nayan, K. Byrappa, *Materials Research Innovations*, 2011, **15**, 36-42.

53 S. Liufu, H. Xiao, Y. Li, *Powder Technol.*, 2004, **145**, 20-24.

54 T. Takagishi, S. Okuda, N. Kuroki, *J. Polym. Sci.- Part A: Polym. Chem.*, 1985, **23**, 2109-2116.

55 D. J. Skrovanek, P. C. Painter, M. M. Coleman, *Macromolecules*, 1986, **19**, Issue no. 3, 699-705.

56 E. Rusu, G. Rusu, D. O. Dorohoi, *Polimery*, 2009, **54**, 347-353.

57 K. J. Kamer, A. Choudhary, R. T. Raines, *J. Org. Chem.*, 2013, **78**, 2099−2103.

58 B. Faure, G. Salazar-Alvarez, A. Ahniyaz, I. Villaluenga, G. Berriozabal, Y. R. De Miguel, L. Bergstr¨om, *Sci. Technol. Adv. Mater.*, 2013, **14,** 023001.

59 G. Fritz, V. Scha¨dler, N. Willenbacher, N. J. Wagner, *Langmuir*, 2002, **18**, 6381-6390.

60 R. Shenhar, T. B. Norsten, V. M. Rotello, *Adv. Mater.*, 2005, **17**, Issue no. 6, 657-669.

61 T. M. Frunze, V. V. Kurashev, L. V. Kozlov, *Russian Chem. Rev.*, 1961, **30**, 252-270.

62 T. K. Dey, R. C. Bindal, S. Prabhakar, P. K. Tewari, *Sep. Sci. and Tech.*, 2011, **46,** 933-943.

63 J. M. M. Peeters, J. P. Boom, M. H. V. Mulder, H. Strathmann, *J. Membr. Sci.*, 1998, **145**, 199-209.

64 M. R. Teixeira, M. J. Rosa, M. Nystrom, *J. Membr. Sci.*, 2005, **265**, 160–166.

65 M. L. Lind, B. H. Jeong, A. Subramani, X. Huang, E. M. V. Hoek, *J. Mater. Res.*, 2009, **24**, 1624-1631.

66 H. Huang, X. Qu, H. Dong, L. Zhang, H. Chen, *RSC Adv.,* 2013, **3**, 8203-8207.

67 T. A. Ostomel, P. K. Stoimenov, P. A. Holden, H. B. Alam, G. D. Stucky, *J. Thromb. Thrombolysis*, 2006, **22**, 55-67.

68 J. Yin, E. S. Kim, J. Yang, B. Deng, *J. Membr. Sci.*, 2012, **423–424**, 238–246.

69 R. X. Zhang, L. Braeken, P. Luis, X. L. Wang, B. Van der Bruggen, *J. Membr. Sci.*, 2013, **437**, 179–188.

70 B. Rajaeian, A. Rahimpour, M. O. Tade, S. Liu, *Desalination*, 2013, **313**, 176–188.

71 G. L. Jadav, P. S. Singh, *J. Membr. Sci.*, 2009, **328**, 257–267.

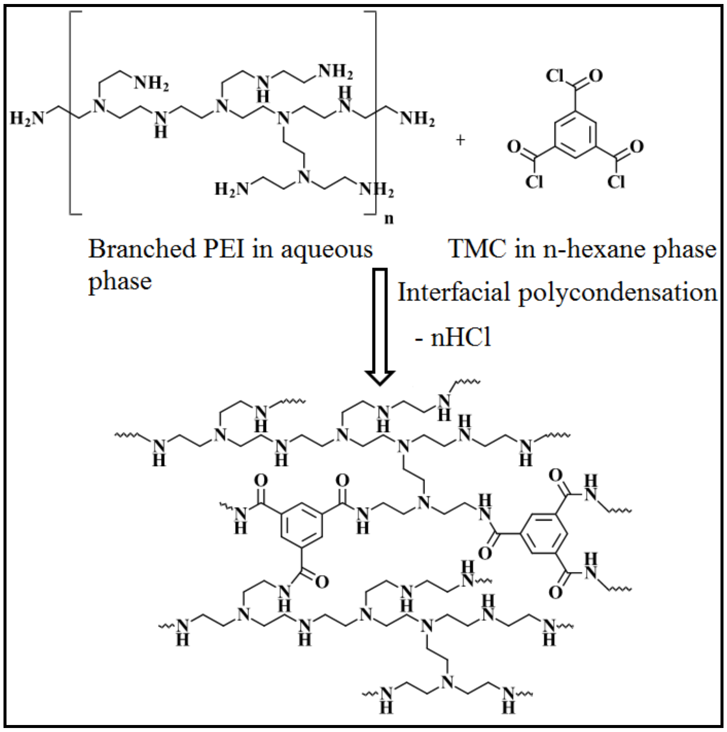

Scheme 1. Synthesis of polyamide from PEI and TMC following *in-situ* interfacial polycondensation process.

Figures

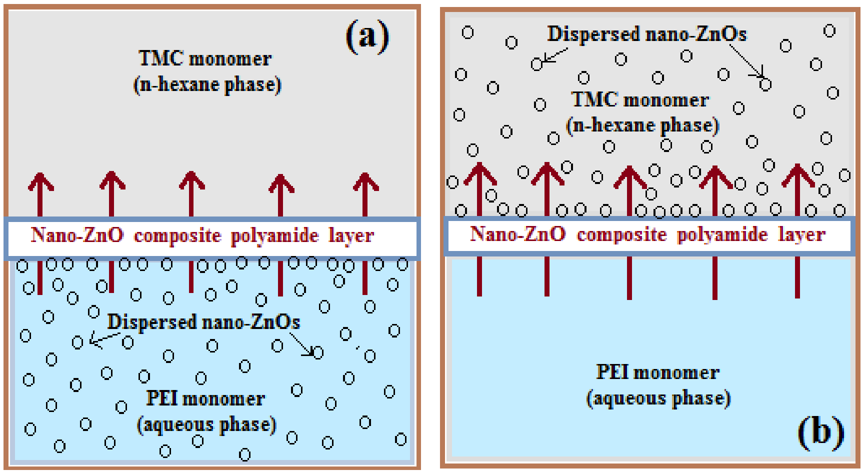

Fig. 1 Schematics of two different pathways: (a) through aqueous phase of PEI and (b) through n-hexane phase of TMC, for nano-ZnO incorporation in the thin skin layer of TFN-NF membranes by *in-situ* interfacial polycondensation process; (The arrows ↑ indicate the direction of diffusion of PEI monomer across the interfacially formed polymeric barrier layer to react with TMC at the organic phase side).

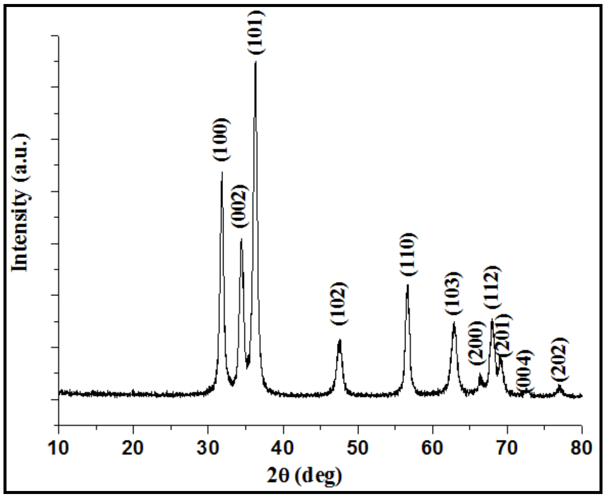

Fig. 2 XRD pattern of as-synthesized nano-ZnO.

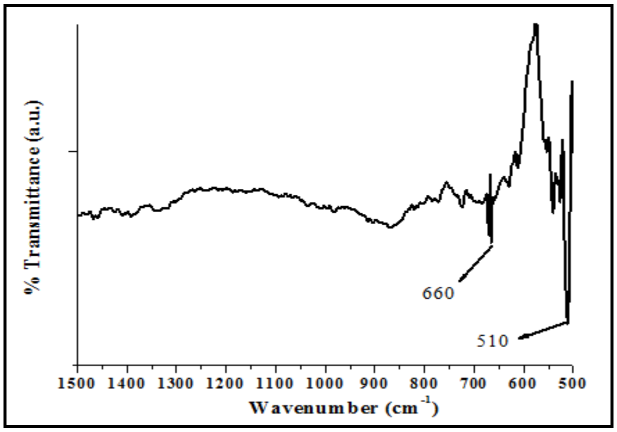

Fig. 3 FTIR spectra for nano-ZnO.

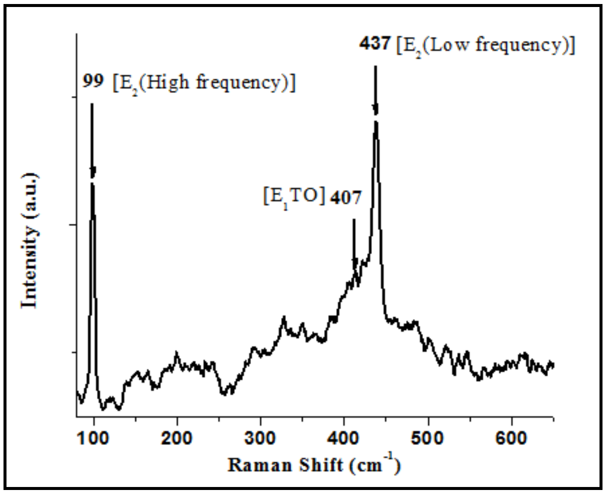

Fig. 4 Room-temperature Raman spectrum for nano-ZnO.

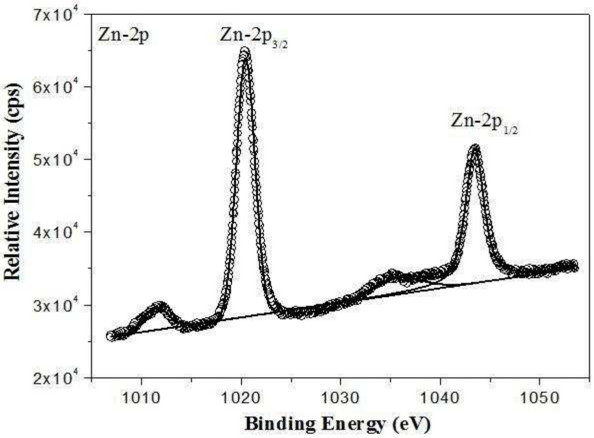

Fig. 5a High resolution Zn-$2p_{3/2}$ and Zn-$2p_{1/2}$ photoelectron spectra obtained from nano-ZnO (line with bullets: experimental data; solid line: curve fit of the experimental data; Zn-$2p_{3/2}$: 1020.5 eV peak contribution and Zn-$2p_{1/2}$: 1043.8 eV peak contribution).

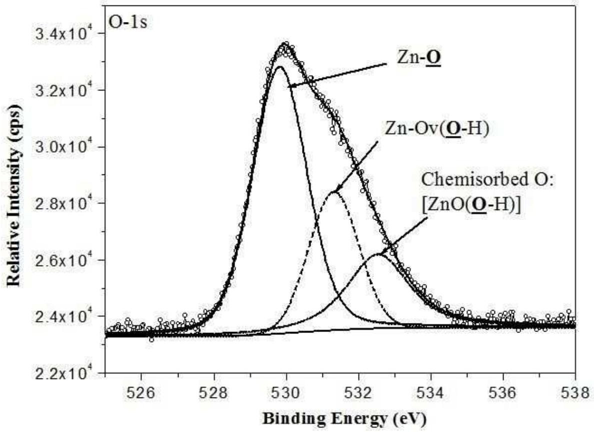

Fig. 5b High resolution O-1s photoelectron spectra obtained from nano-ZnO (line with bullets: experimental data; solid line: curve fit of the experimental data; Zn-**O**: 529.8 eV peak contribution; Zn-Ov(**O**-H): 531.3 eV peak contribution and ZnO(**O**-H): 532.5 eV peak contribution).

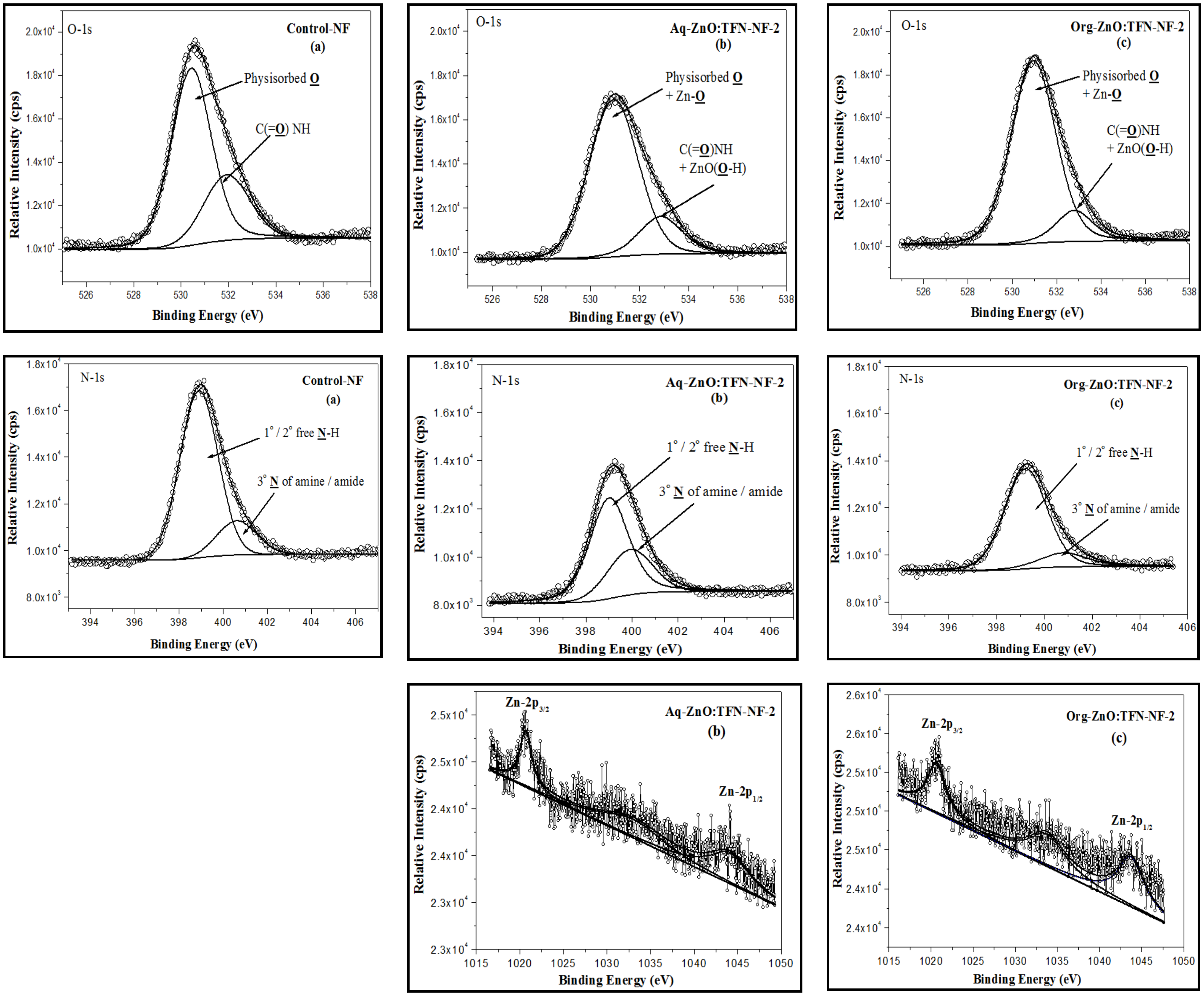

Fig. 6 High resolution O-1s (χ^2: 1.00 - 1.45), N-1s (χ^2: 0.90 - 1.75) and Zn-2p (χ^2: 1.12 - 2.25) photoelectron spectra obtained from nano-ZnO impregnated (a) Control-NF, (b) Aq-ZnO:TFN-NF-2 and (c) Org-ZnO:TFN-NF-2.

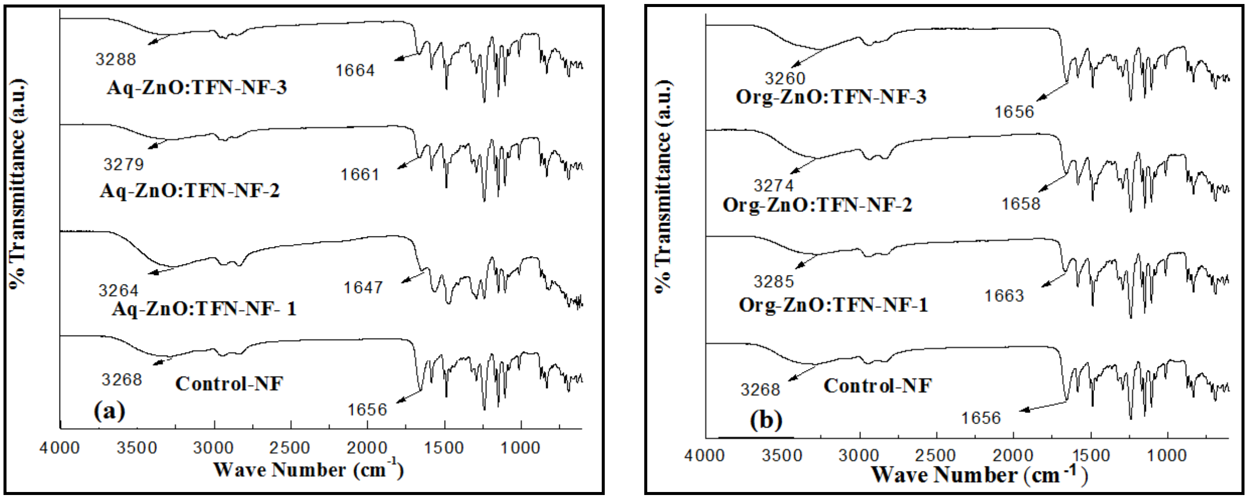

Fig. 7 ATR FT IR spectra of skin layers of TFN-NF membranes: (a) Aq-ZnO:TFN-NF and (b) Org-ZnO:TFN-NF.

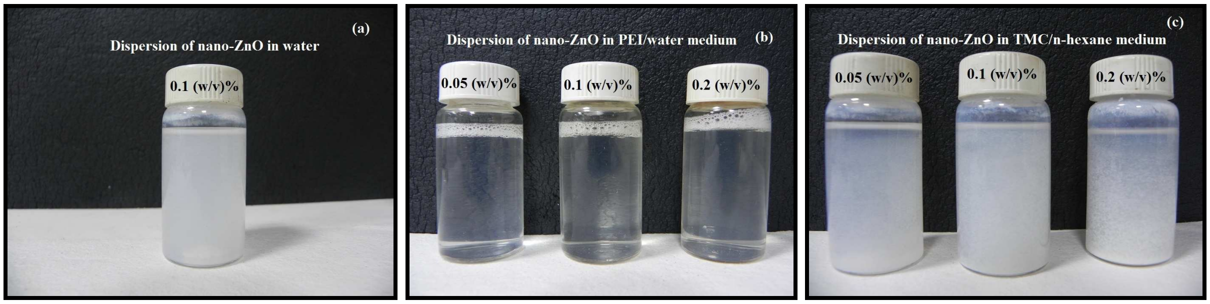

Fig. 8 Photographs of nano-ZnO dispersion (a) in water (without PEI); (b) aqueous phase monomeric-PEI solutions and (c) organic phase monomeric-TMC solutions containing different concentrations of nano-ZnO.

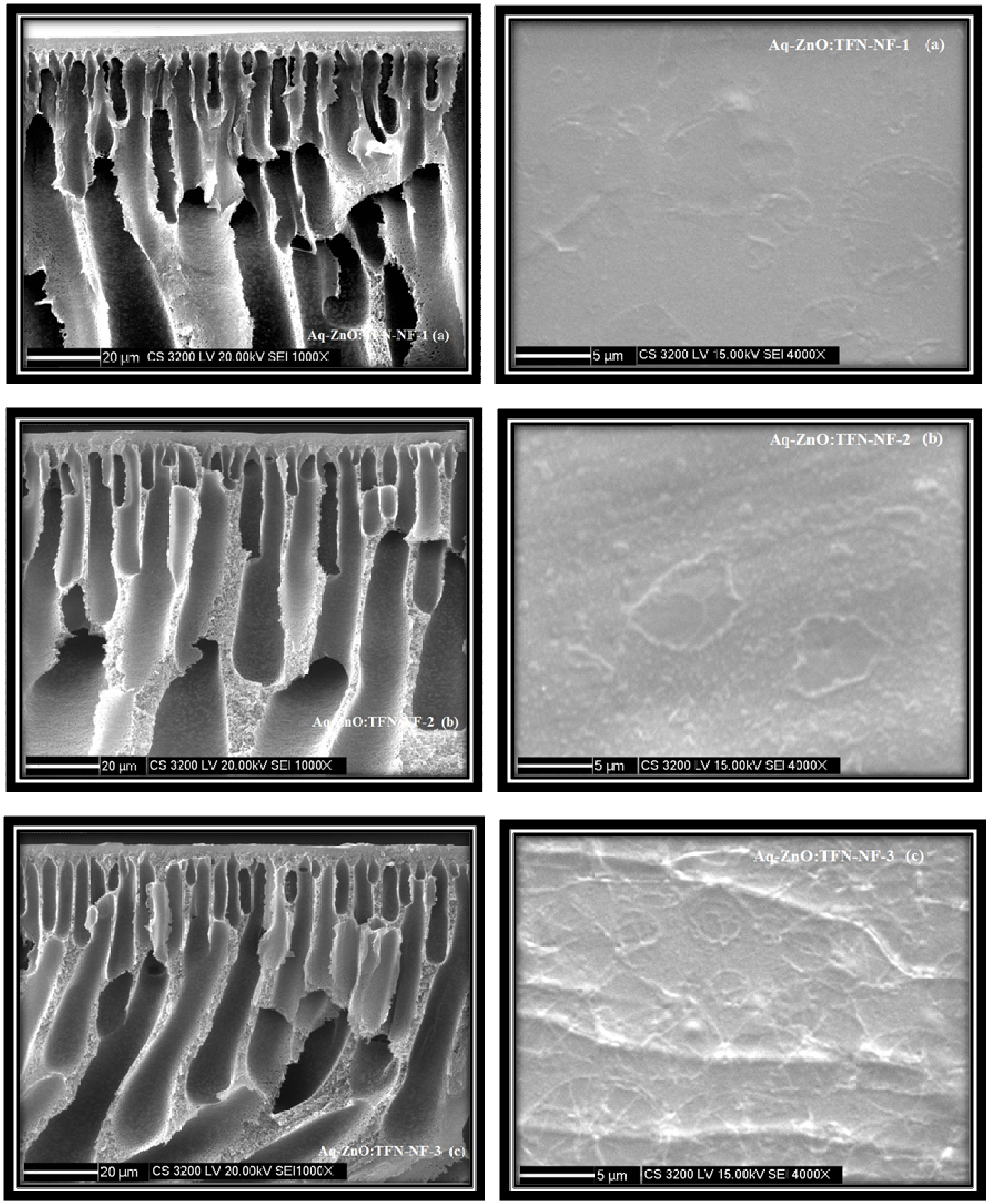

Fig. 9 Cross-sectional and skin surface SEM images of Aq-ZnO:TFN-NF class of membranes made by introducing the nano-ZnO at different concentrations: (a) 0.05 %, (b) 0.1 % and (c) 0.2 % , through aqueous phase containing PEI.

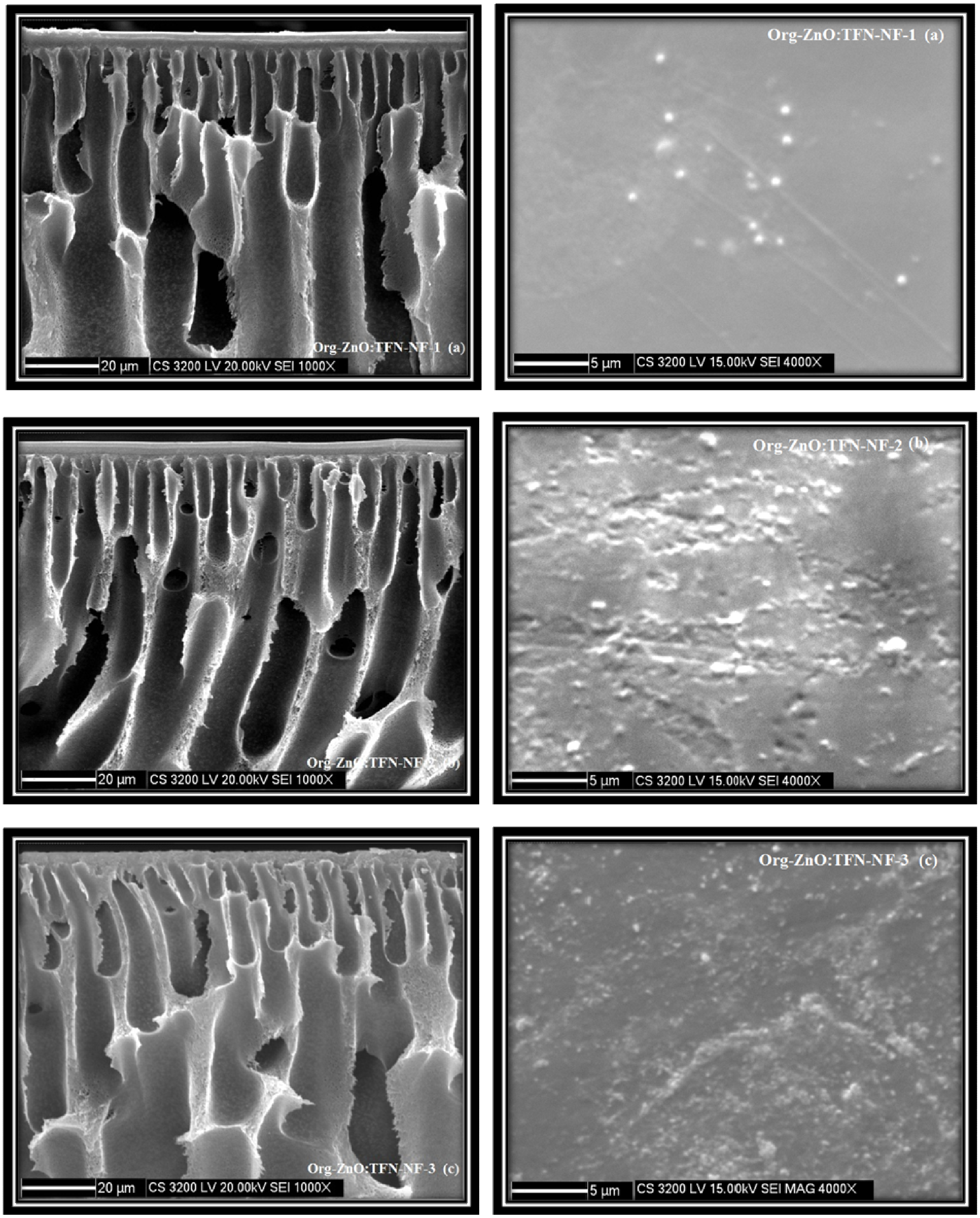

Fig. 10 Cross-sectional and skin surface SEM images of the Org-ZnO:TFN-NF class of membranes made by introducing the nano-ZnO at different concentrations: (a) 0.05 %, (b) 0.1 % and (c) 0.2 % , through organic phase containing TMC.

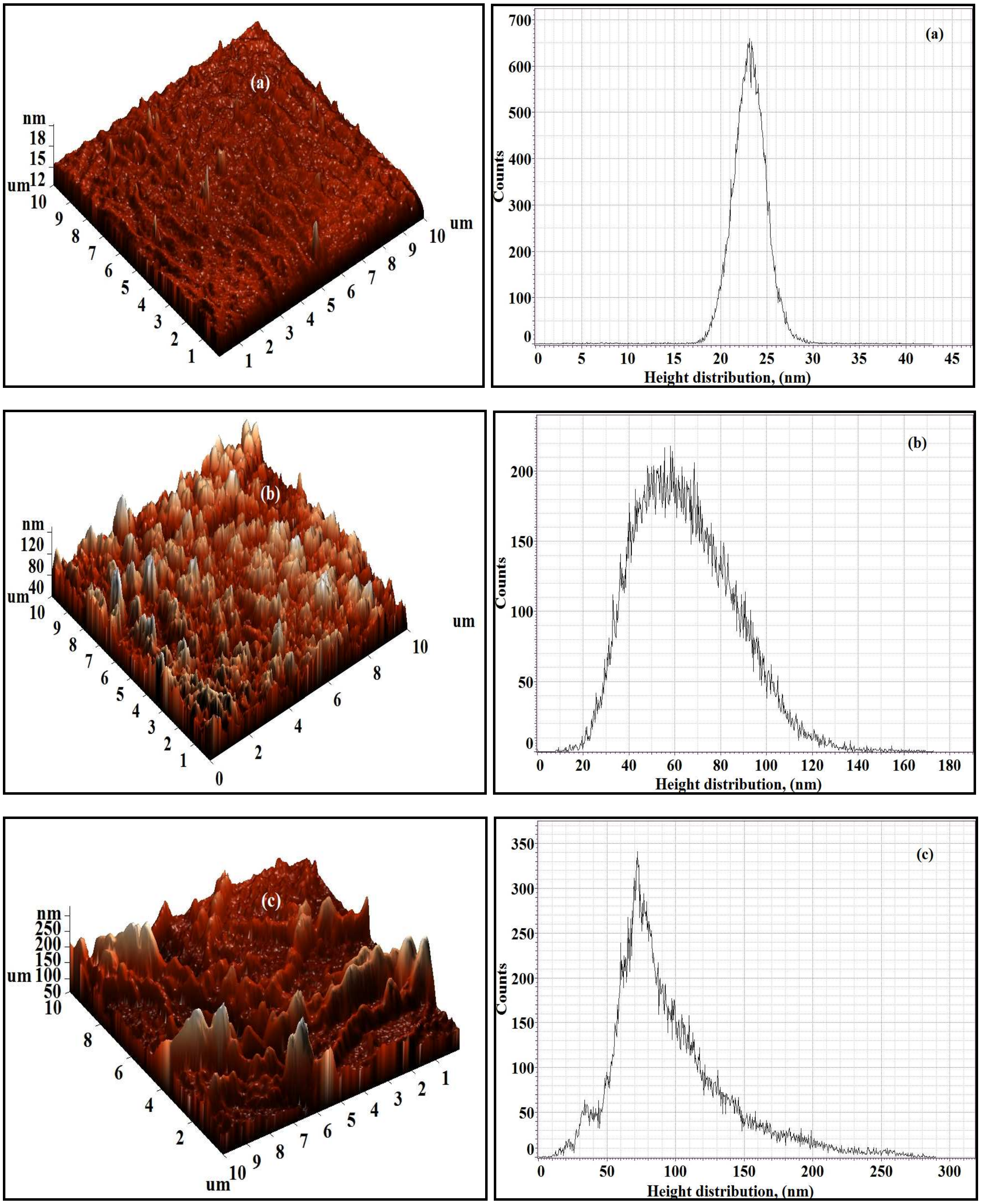

Fig. 11 3D AFM images and height histograms of Aq-ZnO:TFN-NF class of membranes: (a) Aq-ZnO:TFN-NF-1, (b) Aq-ZnO:TFN-NF-2 and (c) Aq-ZnO:TFN-NF-3.

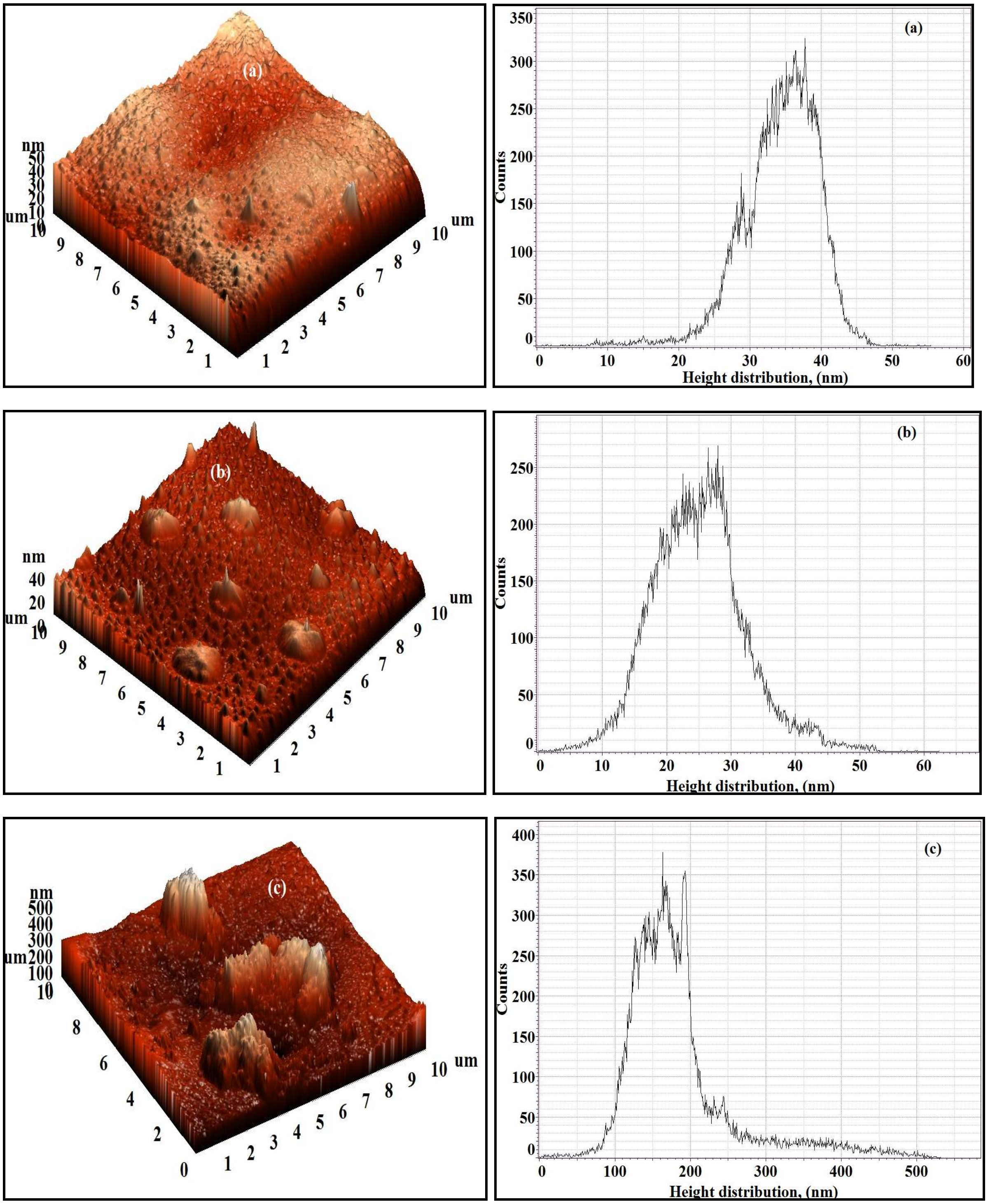

Fig. 12 3D AFM images and height histograms of Org-ZnO:TFN-NF class of membranes: (a) Org-ZnO:TFN-NF-1, (b) Org-ZnO:TFN-NF-2 and (c) Org-ZnO:TFN-NF-3.

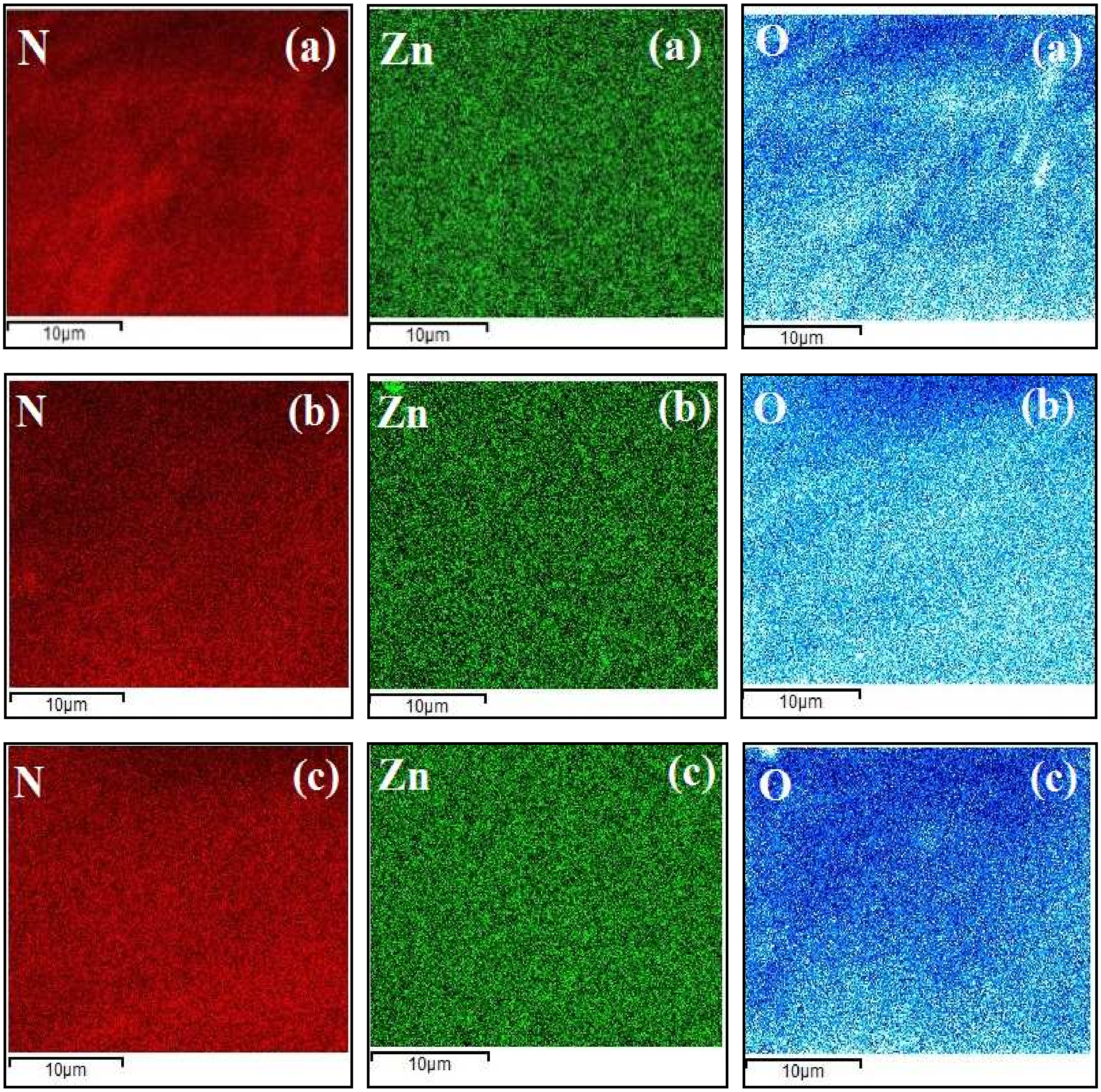

Fig. 13 Elemental mapping of the nanocomposite polyamide skin layers of the Aq-ZnO:TFN-NF class of membranes: (a) Aq-ZnO:TFN-NF-1, (b) Aq-ZnO:TFN-NF-2 and (c) Aq-ZnO:TFN-NF-3.

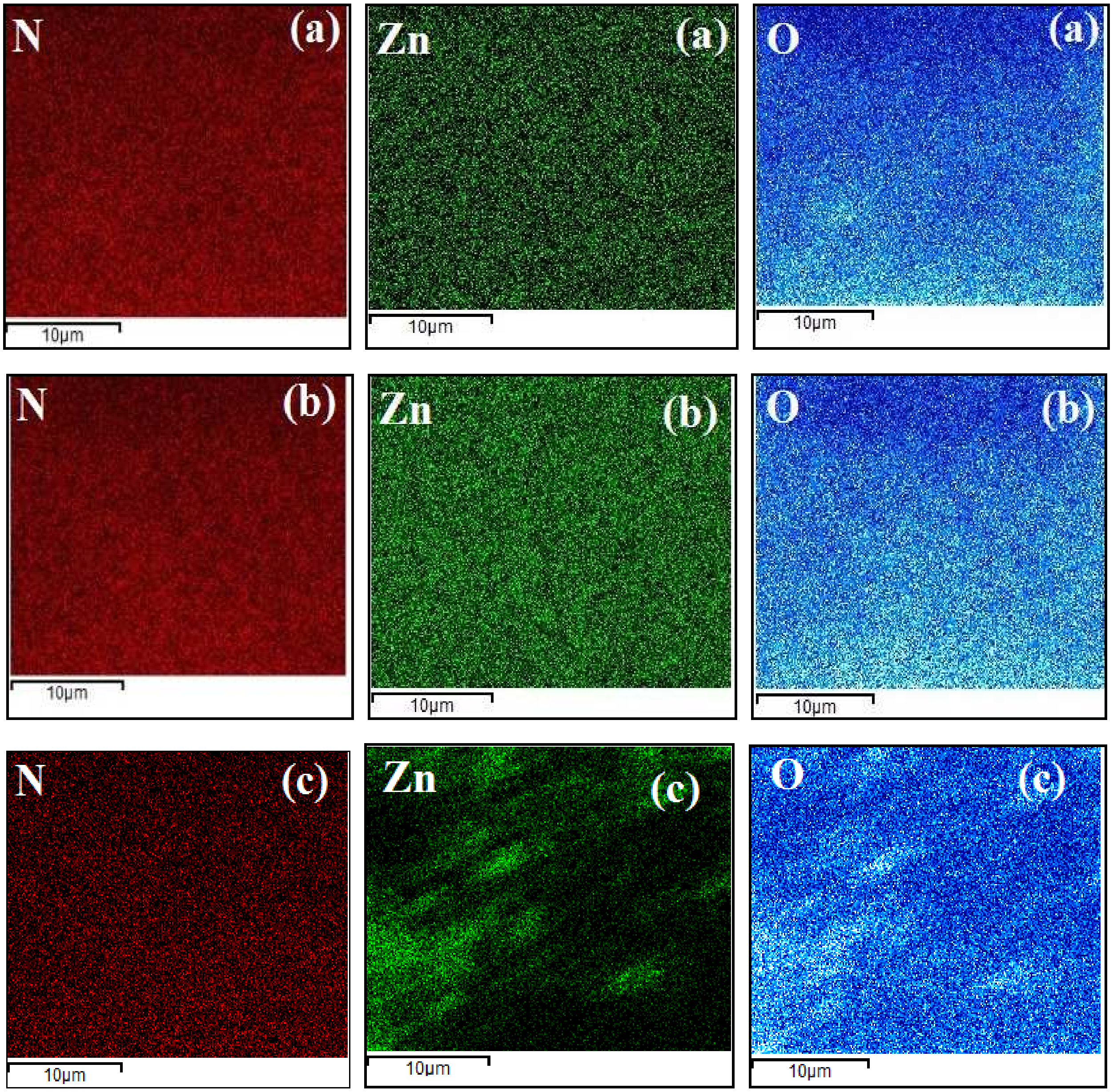

Fig. 14 Elemental mapping of the nanocomposite polyamide skin layers of the Org-ZnO:TFN-NF class of membranes: (a) Org-ZnO:TFN-NF-1, (b) Org-ZnO:TFN-NF-2 and (c) Org-ZnO:TFN-NF-3.

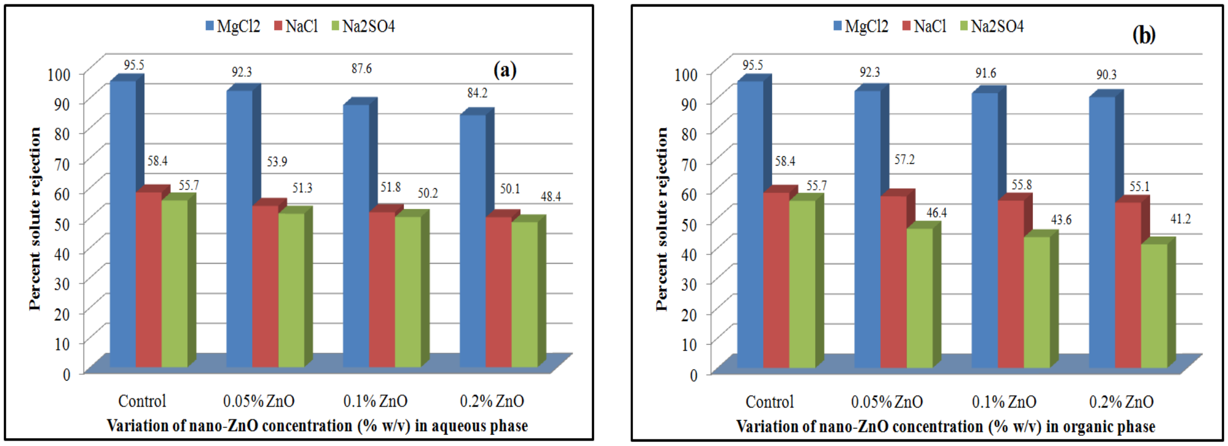

Fig. 15 Effect of variation of nano-ZnO concentration on solute rejection behaviors of (a) Aq-ZnO:TFN-NF and (b) Org-ZnO:TFN-NF class of membranes.

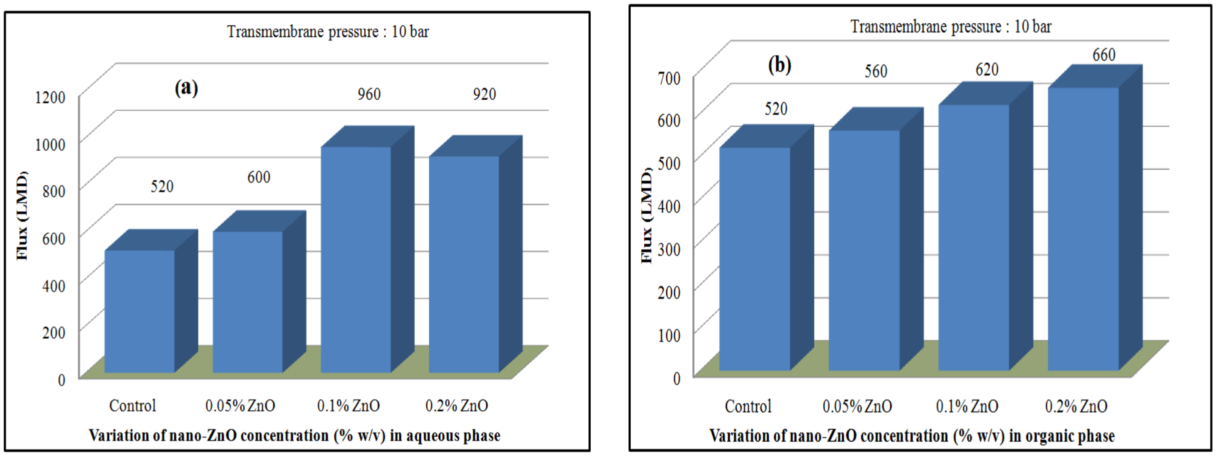

Fig. 16 Effect of variation of nano-ZnO concentration on permeate flux behaviors of (a) Aq-ZnO:TFN-NF and (b) Org-ZnO:TFN-NF class of membranes.

Tables

Table 1 Curve fitting summary of different XPS peaks for skin layers of Control-NF, Aq-ZnO:TFN-NF-2 and Org-ZnO:TFN-NF-2 membranes

Membrane Code	Zn-2p3/2 & Zn-2p1/2			O-1s			N-1s		
	BE (eV)	FWHM (eV)	Peak area (%)	BE (eV)	FWHM (eV)	Peak area (%)	BE (eV)	FWHM (eV)	Peak area (%)
Control-NF		-		530.4	1.99	71.18	398.9	2.04	82.26
				531.9	2.28	28.82	400.6	2.15	17.74
Aq-ZnO:TFN-NF-2	1020.7	1.87	42.29	530.9	2.37	80.88	399.0	2.01	68.24
	1044.0	3.64	57.71	532.8	2.09	19.12	400.0	2.31	31.76
Org-ZnO:TFN-NF-2	1020.6	2.75	40.88	530.9	2.36	86.02	399.2	2.09	84.82
	1043.7	3.94	59.12	532.7	1.99	13.98	400.7	2.40	15.18

Table 2 Computed amplitude parameters for Aq-ZnO:TFN-NF and Org-ZnO:TFN-NF class of membranes by AFM

Membrane Code	Amplitude Parameters		
	Ra (nm)	Rq (nm)	R_{10z} (nm)
Aq-ZnO:TFN-NF-1	1.48	2.09	9.96
Aq-ZnO:TFN-NF-2	17.59	21.96	39.89
Aq-ZnO:TFN-NF-3	31.69	41.96	101.57
Org-ZnO:TFN-NF-1	4.07	5.27	2.58
Org-ZnO:TFN-NF-2	5.58	7.16	9.78
Org-ZnO:TFN-NF-3	49.09	72.23	178.21

Table 3 Skin layer elemental analysis of the Aq-ZnO:TFN-NF & Org-ZnO:TFN-NF class of membranes by EDX

Membrane Code	Elemental (N) quantification		Elemental (O) quantification		Elemental (Zn) quantification		Relative atomic ratio (Zn/N)
	Wt (%)	Atomic (%)	Wt (%)	Atomic (%)	Wt (%)	Atomic (%)	
Aq-ZnO:TFN-NF-1	25.01 ± 0.16	28.17	72.51 ± 0.14	71.19	2.48 ± 0.12	0.64	1:44.02
Aq-ZnO:TFN-NF-2	23.57 ± 0.17	27.52	69.10 ± 0.19	70.65	7.33 ± 0.13	1.83	1:15.04
Aq-ZnO:TFN-NF-3	22.73 ± 0.42	26.42	67.25 ± 0.25	69.93	10.02 ± 0.29	3.65	1:7.24
Org-ZnO:TFN-NF-1	24.87 ± 0.68	28.05	72.08 ± 0.80	71.13	3.05 ± 0.59	0.82	1:34.21
Org-ZnO:TFN-NF-2	22.98 ± 0.28	27.24	67.86 ± 0.32	70.43	9.16 ± 0.20	2.33	1:11.69
Org-ZnO:TFN-NF-3	20.52 ± 0.51	26.07	62.91 ± 0.33	69.53	16.57 ± 0.29	4.40	1:5.93

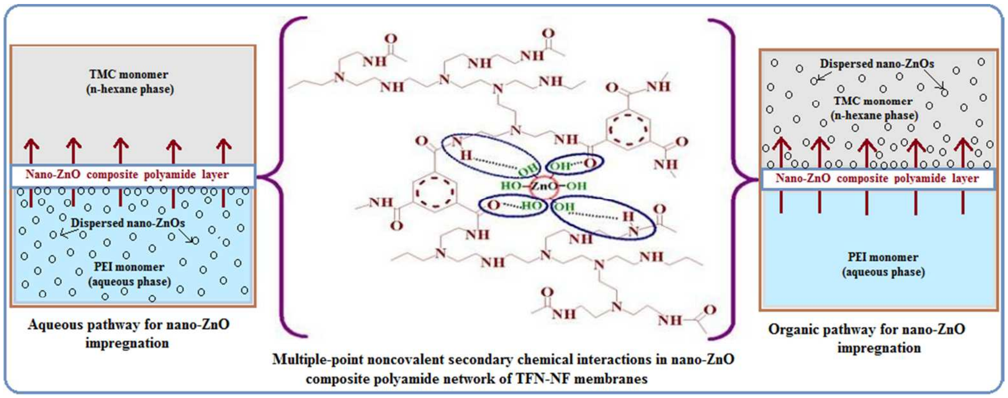

275x107mm (96 x 96 DPI)